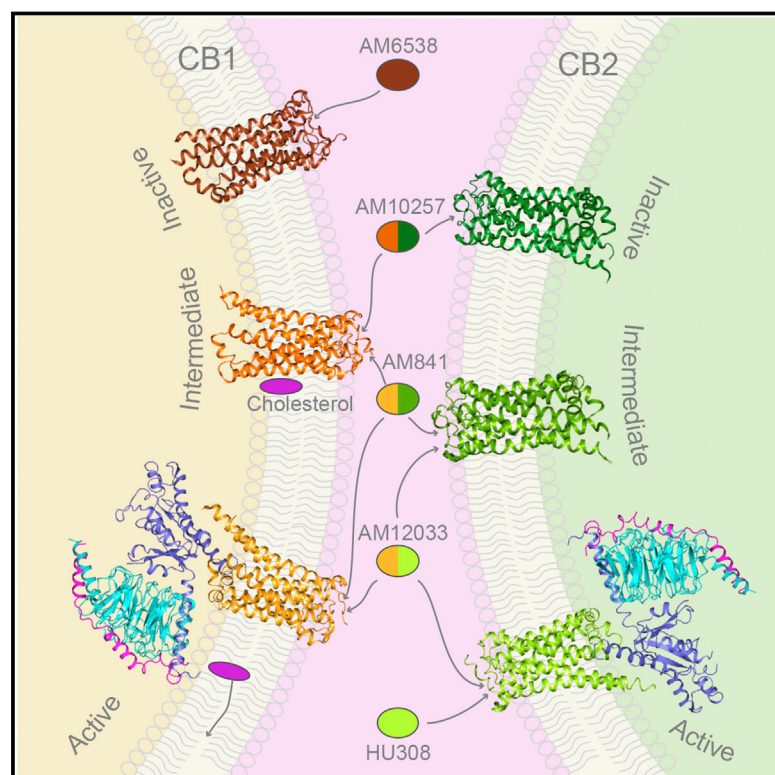# Activation and Signaling Mechanism Revealed by Cannabinoid Receptor-G$_i$ Complex Structures

Graphical Abstract

Authors

Tian Hua, Xiaoting Li, Lijie Wu, ...,
Laura M. Bohn, Alexandros Makriyannis,
Zhi-Jie Liu

Correspondence

huatian@shanghaitech.edu.cn (T.H.),
liuzhj@shanghaitech.edu.cn (Z.-J.L.)

In Brief

Structure and simulations of cannabinoid receptors CB2 and CB1 in their inactive, active-like, and activated signaling states reveal residue differences that may provide G protein selectivity, the distinct binding behavior of CB2 agonists in CB2 and CB1, as well as evidence for modulation of CB1 by cholesterol binding.

Highlights

- 3D structures of CB2-AM12033-G$_i$, CB1-AM841-G$_i$, and CB2-AM12033 are determined

- Structural evidence of G protein selectivity by CB1 and CB2 is identified

- MD simulations reveal the distinct binding behavior of HU308 in CB2 and CB1

- Cholesterol molecule as an endogenous allosteric modulator of CB1 is uncovered

CellPress

Article

Activation and Signaling Mechanism Revealed by Cannabinoid Receptor-G$_i$ Complex Structures

Tian Hua,[1,9,*] Xiaoting Li,[1,9] Lijie Wu,[1,9] Christos Iliopoulos-Tsoutsouvas,[2] Yuxia Wang,[1] Meng Wu,[1,3] Ling Shen,[1,3] Christina A. Johnston,[4] Spyros P. Nikas,[2] Feng Song,[5] Xiyong Song,[6] Shuguang Yuan,[7] Qianqian Sun,[1] Yiran Wu,[1] Shan Jiang,[2] Travis W. Grim,[4] Othman Benchama,[2] Edward L. Stahl,[4] Nikolai Zvonok,[2] Suwen Zhao,[1,3] Laura M. Bohn,[4] Alexandros Makriyannis,[2,8] and Zhi-Jie Liu[1,3,6,10,*]

[1]iHuman Institute, ShanghaiTech University, Shanghai 201210, China
[2]Center for Drug Discovery and Department of Pharmaceutical Sciences, Northeastern University, Boston, MA 02115, USA
[3]School of Life Science and Technology, ShanghaiTech University, Shanghai 201210, China
[4]Departments of Molecular Medicine and Neuroscience, Scripps Research, Jupiter, FL 33458, USA
[5]School of Life Science, Dezhou University, Dezhou 253023, Shandong Province, China
[6]Institute of Molecular and Clinical Medicine, Kunming Medical University, Kunming 650500, Yunnan Province, China
[7]The Research Center for Computer-aided Drug Discovery, Shenzhen Institutes of Advanced Technology, Chinese Academy of Sciences, Shenzhen 518055, China
[8]Center for Drug Discovery and Departments of Chemistry and Chemical Biology, Northeastern University, Boston, MA 02115, USA
[9]These authors contributed equally
[10]Lead Contact
*Correspondence: huatian@shanghaitech.edu.cn (T.H.), liuzhj@shanghaitech.edu.cn (Z.-J.L.)
https://doi.org/10.1016/j.cell.2020.01.008

SUMMARY

Human endocannabinoid systems modulate multiple physiological processes mainly through the activation of cannabinoid receptors CB1 and CB2. Their high sequence similarity, low agonist selectivity, and lack of activation and G protein-coupling knowledge have hindered the development of therapeutic applications. Importantly, missing structural information has significantly held back the development of promising CB2-selective agonist drugs for treating inflammatory and neuropathic pain without the psychoactivity of CB1. Here, we report the cryoelectron microscopy structures of synthetic cannabinoid-bound CB2 and CB1 in complex with G$_i$, as well as agonist-bound CB2 crystal structure. Of important scientific and therapeutic benefit, our results reveal a diverse activation and signaling mechanism, the structural basis of CB2-selective agonists design, and the unexpected interaction of cholesterol with CB1, suggestive of its endogenous allosteric modulating role.

INTRODUCTION

Cannabinoid receptors CB1 and CB2 serve as key components of the endocannabinoid system and are the principal targets of Δ^9-tetrahydrocannabinol (Δ^9-THC), a psychoactive chemical from *Cannabis sativa* with a wide range of therapeutic applications (Lemberger, 1980). CB1 and CB2 play crucial roles in a variety of physiological processes, including appetite, pain sensation, memory, and immunomodulation (Guzmán, 2003). The two cannabinoid receptors share 44% total sequence iden-

tity and 68% sequence similarity in the transmembrane regions (Munro et al., 1993). However, they differ in their tissue distribution and exert distinct functions in endocannabinoid system, where CB1 and CB2 are expressed predominantly in the central nervous system and the immune system, respectively.

So far, several crystal structures of cannabinoid receptors have been determined, including antagonist-bound (Hua et al., 2016; Shao et al., 2016) and agonist-bound CB1 (Hua et al., 2017) as well as antagonist-bound CB2 structures (Li et al., 2019). While these structures have enhanced our understanding of the ligand induced inactive or active-like states, there are a number of important challenges that remain. First, the development of therapeutic applications has been hindered by difficulty in specifically modulating the individual cannabinoid receptors due to their high sequence similarity. Also, the absence of the agonist-bound CB2 structure has held back the development of CB2-selective agonists as high potential drug candidates for treating inflammatory and neuropathic pain without the psychoactivity of CB1 (Contino et al., 2017; Lunn et al., 2008).

Finally, CB2 and CB1 elicit their physiological responses by coupling primarily to G$_{i/o}$ proteins to inhibit adenylate cyclase and cyclic AMP signaling, yet CB1 also couples with G$_s$ (G protein-stimulating adenylate cyclase) or G$_{q/11}$ (G protein-activating phospholipase C and G protein-increasing cytosolic Ca^{2+}) to instigate signaling under special circumstances (Glass and Felder, 1997; Lauckner et al., 2005). Although an indole-based synthetic cannabinoid MDMB-Fubinaca (FUB)-bound CB1-G$_i$ structure was determined recently (Krishna Kumar et al., 2019), the activation and G protein-coupling mechanism underlying the two cannabinoid receptors CB2 and CB1 is still elusive.

Here, we have used single-particle cryoelectron microscopy (cryo-EM) and obtained the structures of agonist-bound CB2 and CB1 in complex with the heterotrimeric protein G$_i$ as well as the crystal structure of agonist-bound CB2 by X-ray crystallography method. Together with our previously reported crystal
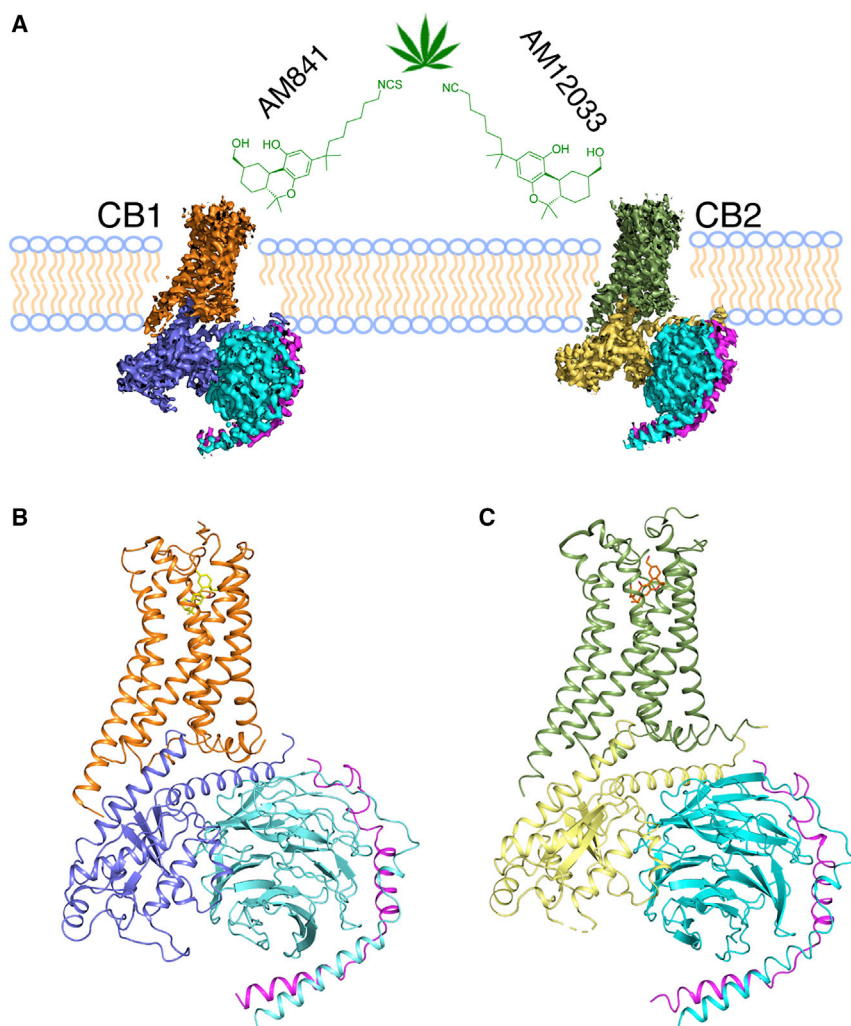
Figure 1. Cryo-EM Structures of the CB1-G$_i$ and CB2-G$_i$ Complexes

(A) Cryo-EM density maps of the CB1-G$_i$ and CB2-G$_i$ complexes, with colored subunits. Color code for the proteins is as follows: CB1, orange; CB2, green; Gα_i in CB1, slate; Gα_i in CB2, yellow; G$_\beta$, cyan; G$_\gamma$, magenta.

(B and C) Cryo-EM structures of CB1-G$_i$ (B) and CB2-G$_i$ (C) complexes using same color code as in (A), with AM841 and AM10233 shown as yellow and orange sticks, respectively.

See also Figure S2 and Table S1.

(K_i = 0.37 nM for CB2) agonist AM12033 (Figure S1). The CB2-G$_i$ complex was further stabilized by the addition of scFv16 (Koehl et al., 2018). Single-particle cryo-EM analysis of the frozen sample enabled us to obtain nominal global maps at 2.9 Å resolution for CB2-AM12033-G$_i$-scFv16 (Figure 1; Figure S2; Table S1). The ligand, receptor, and G$_i$ in the isolated complex are clearly visible in the EM maps (Figure S2). Side chains of the majority of amino acid residues are well defined in all protein components (Figures S2C and S2D). Thus, the structure provides an accurate model of intermolecular interactions of CB2 with the agonist and G$_i$.

The same method was applied in obtaining the CB1-AM841-Gi-scFv16 complex cryo-EM structure at 3.0 Å resolution and the only differences is that the CB1-G$_i$ complex was constituted *in vitro* from purified protein components using the THC-like cannabinoid agonist AM841(Hua et al., 2017) instead of *in vivo* co-expression for CB2-Gi complex. In addition, the agonist AM12033-bound CB2 crystal structure was also determined at 3.2 Å resolution (Table S2).

structures of CB1 and CB2, we have, so far, determined structures of CB1 and CB2 in their inactive, active-like, and active states. Comparing the six cannabinoid receptor structures together with several other solved G protein-coupled receptor (GPCR) structures in complex with G$_{i/o}$, G$_s$, or G$_{11}$ proteins, this study provides comprehensive insights into the diverse activation and means by which cannabinoid receptors couple to G proteins and opens up avenues for the rational design of new selective ligands, especially agonists, to precisely modulate the endocannabinoid systems.

RESULTS

Solution of CB2-Gi Cryo-EM Structure and Agonist-Bound CB2 Crystal Structure

To prepare the stable CB2-G$_i$ (G$\alpha_i\beta\gamma$) complexes for cryo-EM studies, we tried different modifications and ligands. Eventually, the expression level of CB2 receptor was improved by the insertion of BRIL protein at CB2's N terminus. The stability of the CB2-G$_i$ complex was achieved by co-expression of the receptor with the heterotrimeric G$_i$ protein and the designed high-affinity

Overall Structure of CB2 Signaling Complex and Its Comparison with CB1-Gi Complex

The overall structure of the active CB2-G$_i$ complex is similar to that of the active conformation of the CB1-G$_i$ complex (Figure 2A), with root mean square deviation (RMSD) values of 1.65 Å for the whole complex, 1.26 Å for the receptors alone, and 0.41 Å for the G$_i$ proteins. The N termini of both receptors adopt identical conformations, forming a short helix over the binding pocket. The binding poses of AM12033 in CB2 and AM841 in CB1 are superimposable. When comparing inactive and active states of CB2, we observe an outward movement of TM6 that is characteristic of receptor activation and an extension of TM5 that resulted in new interactions with Gα_i (Figure 2B). Similar conformational changes are also observed in CB1-G$_i$ complex structure (Figures S3A and S3B). These structural changes allow the G protein to engage with the receptor core.
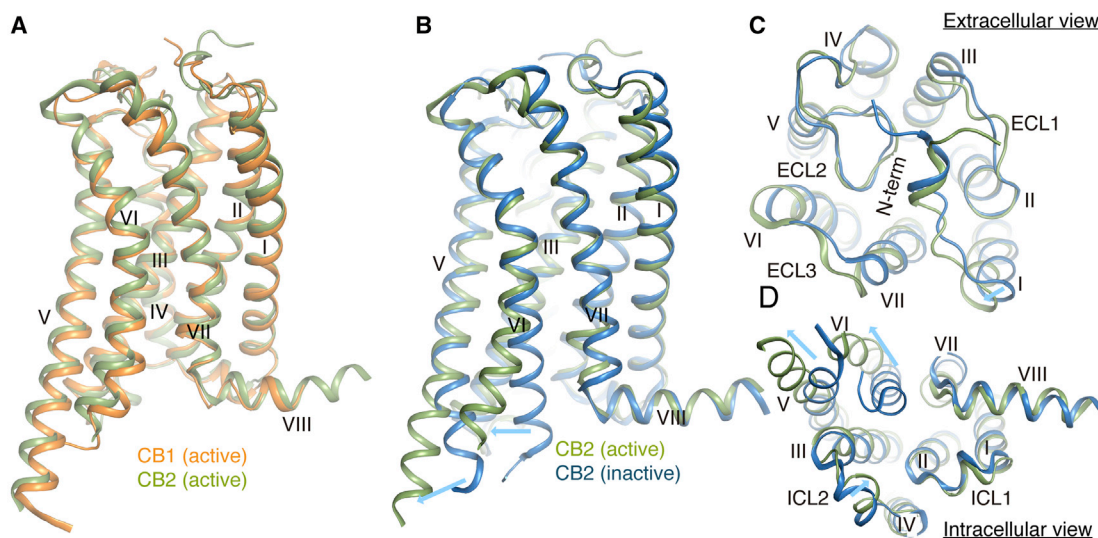
Figure 2. Comparison of Cannabinoid Receptor Structures
(A) Comparison of active CB1, orange; and CB2, green.
(B–D) Side (B), extracellular (C), and intracellular (D) comparison views of active, green; and inactive, sky blue (PDB: 5ZTY) CB2 structures. Conformational changes are indicated with blue arrows.
See also Figure S3.

In addition, the conformations of critical residues for the receptor activation, such as $D^{3.49}R^{3.50}Y^{3.51}$ and $N^{7.49}P^{7.50}xxY^{7.53}$ motifs (superscripts indicate Ballesteros-Weinstein numbering for GPCRs [Ballesteros and Weinstein, 1995]), are almost identical between the active conformations of CB2 and CB1 (Figures S3C and S3D). Different from the large conformational changes of both extracellular and intracellular domains occurring from inactive to active states in CB1 (Figure S3B), the extracellular region, including the N terminus of CB2, undergoes very minor changes during its activation (Figures 2C and 2D).

The overall structure of the G_i heterotrimers in CB2 and CB1 complex structures is similar to those previously solved GPCR-G_i complexes (Figure S4). No electron density for guanosine diphosphate (GDP) is observed in the GDP-binding pocket, which is mainly formed by the $\beta1$-$\alpha1$ loop (P loop) and the $\beta6$-$\alpha5$ loop, suggesting that G_i is nucleotide-free in both receptor-G_i complex structures. The antibody scFv16 binds at a similar interface comprising of the αN helix of $G\alpha_i$ and the β-propeller of $G\beta$, as previously reported (Koehl et al., 2018).

The Interactions between CB2 and G_i
The structure of the CB2-G_i complex reveals a similar mode of interaction when compared with the CB1-G_i complex. The contacts between CB2 and G_i are extensively mediated through the $G_{\alpha i}$ subunit. The primary interaction interface is composed of TM3, TM5, TM6, and ICL2 of the receptor and the $\alpha5$ helix, αN helix, and αN-$\beta1$ loop of the $G\alpha_i$ subunit (Figure 3A). Similar to other G_i-bound GPCRs, the two large hydrophobic side chains L353 and L348 of the $\alpha5$ helix from $G\alpha_i$ are directed toward the hydrophobic pocket. For example, the hydrophobic pocket is formed by Val212$^{5.61}$, Leu243$^{6.33}$, Leu247$^{6.37}$, Leu239$^{6.29}$, and Leu135$^{3.54}$ from the cytosolic ends of TM5, TM6, and TM3 of re-

ceptor (Figure 3B). However, compared to the μOR-, A1-, 5HT1B-, and M2-G_i complexes (Draper-Joyce et al., 2018; García-Nafría et al., 2018; Koehl et al., 2018; Maeda et al., 2019), the G_i proteins in CB2- and CB1-G_i complexes are observed to have a ~20° anticlockwise rotation (if viewed from intracellular to extracellular direction) when aligning all available receptor-G protein complex structures using CB2 structure as reference (Figures S4A and S4B). The orientation difference of the G_i proteins from CB2 and CB1 complexes may be attributed to the more extended TM5 of CB2 or CB1 where additional interactions with the $\alpha5$ helix of $G\alpha_i$ are observed (Figure 3B). Specifically, residues Ser222$^{5.71}$ and His226$^{5.75}$ from CB2 or R311$^{5.75}$ from CB1 formed new interactions with D337 and Q333 in $\alpha5$ helix of $G\alpha_i$. We hypothesize that the extra pulling force may serve to twist G_i into a more energy-favorable orientation in the CB2- and CB1-G_i complexes.

While CB1 and CB2 signal through G_i, CB1 is also known to couple with G_s or G_q. After careful inspection of the residues that are involved in the receptor-G_i interactions, L222^{ICL2} in CB1 is found in the proximity of L194 in the $\beta2$-$\beta3$ loop, as well as I344 in $\alpha5$ helix of $G\alpha_i$, which established weak interactions between CB1 and G_i (Figure 3C). In contrast, equivalent residue to L222^{ICL2} in CB2 is P139^{ICL2}, which is unique in class A GPCRs and not involved in the interaction with G_i (Figure 3C). Previous studies have shown that the P139^{ICL2} mutation of P139F, P139M, or P139L enabled CB2 to couple with G_s protein (Zheng et al., 2013). In addition, the L222^{ICL2} (CB1) equivalent residue F139^{ICL2} in the β_2AR-G_s structure forms extensive hydrophobic interactions with a pocket consisting of $\alpha5$ helix, $\beta2$-$\beta3$ loop, and $\beta1$ strand in $G\alpha_s$ (Figures S4E and S4F) (Maeda et al., 2019). In agreement, L222F mutation in CB1 has been shown to increase CB1-G_s basal activity (Chen et al., 2010b; Krishna Kumar et al., 2019). Thus, we speculate that the residue
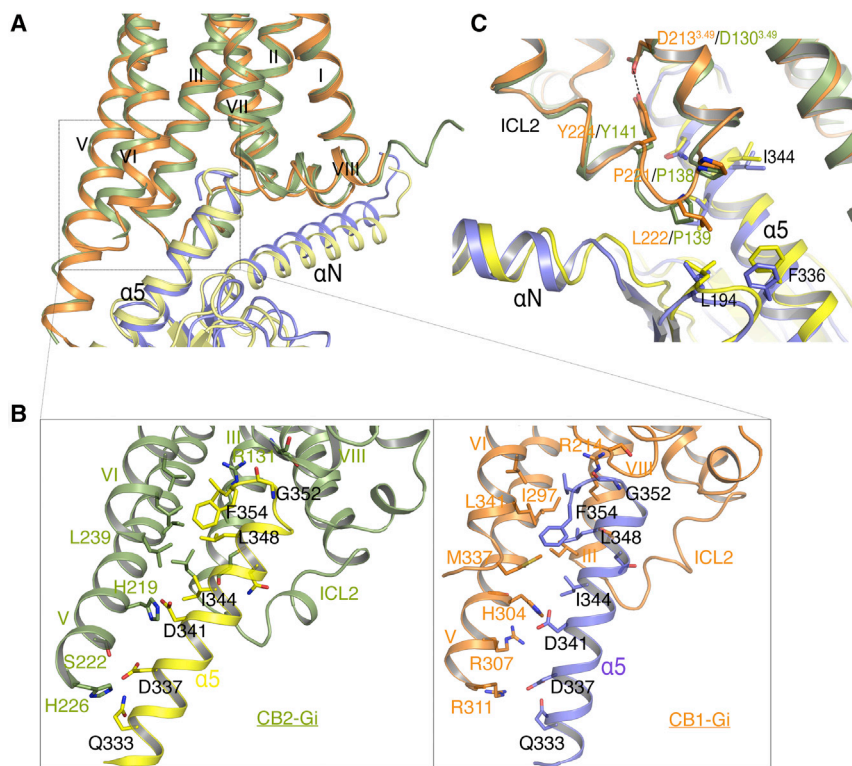
Figure 3. Comparison of CB1-G$_i$ and CB2-G$_i$ Binding Interfaces

(A) Conformation comparison of the α5 helices (CB1-G$_i$, blue; CB2-G$_i$, yellow) in Gα$_i$ and receptors (CB1, orange; CB2, green) in CB1-G$_i$ and CB2-G$_i$ complexes when aligned on the receptors.

(B) Interactions between the α5 helix in Gα$_i$ and TM3, TM5, and TM6 in CB1 or CB2 (same color code).

(C) Interactions between Gα$_i$ and ICL2 of CB1 and CB2 (colors as in A).

See also Figure S4.

(Figure S5A). Notably, the binding pockets of agonist AM12033 and antagonist AM10257 in CB2 share a high degree of similarity, as speculated in our previous report (Li et al., 2019) (Figure 4C), while the inward movements of extracellular parts of TM1, TM4, and TM7 produce a more compact agonist-binding pocket in CB2.

Diverse Activation Processes of CB2 and CB1

In the AM12033-G$_i$-bound CB2 structure, the side chain of "toggle switch" residue Trp258[6.48] experiences an expected major conformational change (Figure 4D) and a large outward movement of the intracellular part of TM6 by 11 Å (Arg238 as reference) to accommodate the mounting of α5 from the Gα$_i$ protein (Figure 5A). Moreover, the cytoplasmic portion of TM5 extended and moved outward by about 6 Å (V220 as reference) to form extensive interactions with the α5 of the Gα$_i$, as discussed above. However, the cytoplasmic region of TM5 in CB1 is simply extended during activation (Figure 5B). The larger movement of TM5 in CB2 may be attributed to Gly210[5.59] (Met295[5.59] in CB1) that provides extra bending flexibility of TM5 (Figure 5C). Additionally, the classical activation features in class A GPCRs are also observed here, including the rearrangement of "microswitches" DRY and NPxxY motifs (Figures S3C and S3D) (Erlandson et al., 2018). The "ionic lock" between Arg131[3.50] and Asp240[6.30], which is important for maintaining the ground state of the receptor (Savinainen et al., 2003), is broken, and Arg131[3.50] in the DRY motif extends toward TM7 and forms a hydrogen bond with G352 from the α5-helix of G$_{zi}$. A 4 Å inward displacement of the NPxxY motif (N295[7.49], P296[7.50], and Y299[7.52]) in TM7 induces the conformational change of helix 8 and ICL1, eventually leading to the closer interaction between the receptor and G$_i$.

The overall structure of AM841-CB1-G$_i$ is similar to our previously solved AM841-bound CB1 crystal structure (Hua et al., 2017). The main differences occur in the CB1-G protein interface where the interacting residues are stabilized by G$_i$. In addition, elongation of TM5 and inward movement of TM5, TM6, ICL1, and ICL2 in the intracellular region resulted in more polar and hydrophobic interactions with α5 of the Gα$_i$ protein (Figure S5D). The binding poses of AM841 in the two structures are almost

L222[ICL2] in CB1 facilitates its coupling with G$_s$, and likely G$_q$ as well.

Concerning the interactions between ICL1, helix8 from CB2 and Gα$_i$, we identified that Ser69 and Tyr70 in ICL1 form polar interactions with D305 in Gα$_i$, which constrain the conformation of ICL1. In addition, ICL1 and helix8 of CB2 are in close proximity to the G$_\beta$ subunit, and the presence of multiple polar and charged amino acids at this interface suggests potential interactions.

AM12033-CB2 Interactions Unveiled by Cryo-EM and Crystal Structures

In the CB2-G$_i$ complex, the agonist AM12033 adopts an L-shape conformation in the orthosteric binding pocket. The interactions between AM12033 and CB2 are mainly hydrophobic and aromatic, including residues from ECL2, TM3, TM5, TM6, and TM7 (Figure 4). The tricyclic tetrahydrocannabinol system of AM12033 forms π-π interactions with Phe183[ECL2], Phe281[7.35] and Phe94[2.64], and the phenolic hydroxyl at C1 forms a hydrogen bond with Ser285[7.39]. The alkyl chain of AM12033 extends into the long channel and forms hydrophobic interactions with residues from TM3, TM5, and TM6. Prior to solving cryo-EM CB2-G$_i$ complex structure, we have already determined the AM12033-bound CB2 crystal structure at 3.2 Å resolution (Figure 4A) where the binding pose of AM12033 can be unambiguously defined, owing to the clear electron density in the orthosteric ligand-binding pocket. The competitive binding of AM12033 is in agreement with cyclic adenosine monophosphate (cAMP) functional assay (Figures S3E and S3F). The agonist AM12033 in both cryo-EM and crystal structures shares almost identical binding poses, and the surrounding residues take similar conformations as well
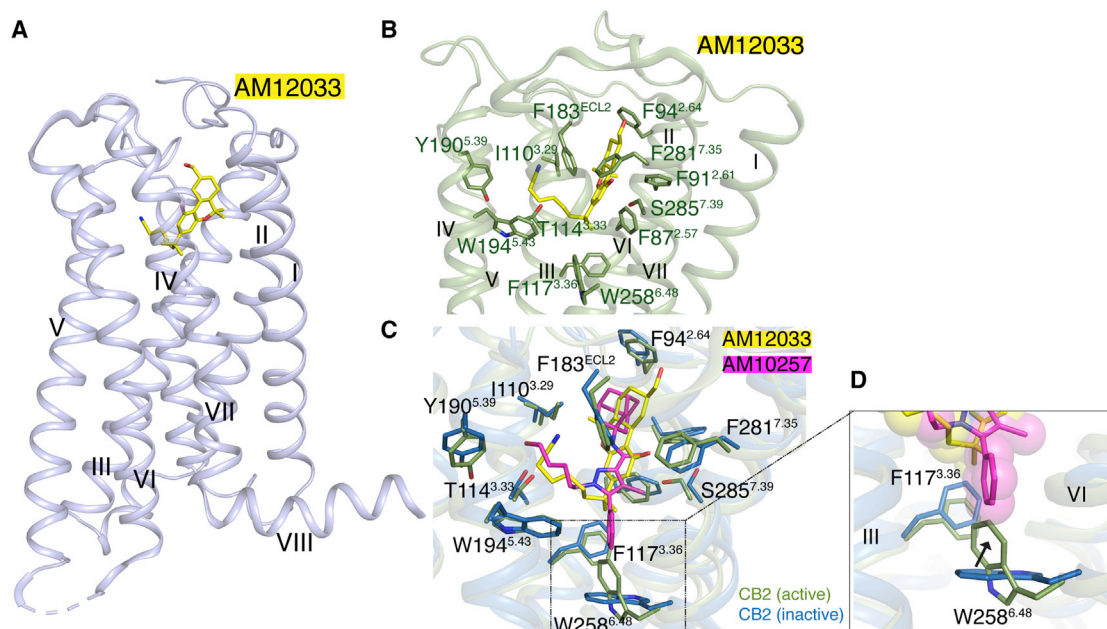
Figure 4. AM12033-Bound CB2 Crystal Structure and Interactions between AM12033 and CB2

(A) Crystal structure of AM12033, yellow sticks; bound CB2, light blue cartoon.

(B) Key residues, green sticks, involved in AM12033, yellow sticks, binding in CB2-G$_i$ complex structure, green cartoon.

(C) Binding poses comparison of AM12033, yellow sticks; and AM10257, magenta sticks in CB2.

(D) Comparison of the "toggle switch" residue conformation in active, green cartoon; and inactive, sky blue cartoon, CB2.

See also Figures S1 and S5 and Table S2.

indistinguishable in the orthosteric binding pocket along with the key interacting residues. The "twin toggle switch" residues Phe200$^{3.36}$ and Trp356$^{6.48}$ adopt similar conformation in the two structures (Figure S5E), confirming their important role in CB1 activation. The DRY and NPxxY motifs show similar rearrangements (Figure S5F), indicating that the AM841-bound CB1 crystal structure is close to the active state. In contrast to the agonist-bound CB1 structures, the intracellular regions of TM5, TM6, and TM7 adopt a more converged conformation in AM12033-bound CB2 crystal structure, and its overall C$_\alpha$ RMSD with antagonist AM10257-bound CB2 is only 0.86 Å (Figure S5C), compared with CB2-G$_i$ complex structure (Figure S5B). In our previous study, we have shown that class A GPCRs exhibit very diverse conformational changes in the intracellular region in responding to agonist binding (Hua et al., 2017). CB2 behaves as most solved class A GPCRs, which only experience minor conformational changes upon agonist binding, while CB1 is exceptional and displays larger conformational changes when modulated by agonists.

The structures (inactive, agonist-bound, and active states) of CB2 and CB1 we have obtained so far reveal intriguing conformational diversities (Figures 5A and 5B) and provide us the structural basis for deciphering the activation and signaling mechanism of cannabinoid receptors. First, the balloon-like plasticity of CB1 during the transitions between different states facilitates its inherent ability to respond to a diverse array of ligands compared to CB2. More interestingly, the two closely related receptors experience quite different activation processes. The more complicated activation of CB1 assumes the synergistic conformational change of the "twin toggle switch,"

Phe3.36 and Trp6.48, to unleash the large conformational changes and induce the G protein-coupling. Yet in CB2, the single "toggle switch," Trp6.48, is enough to trigger the activation and the downstream signaling.

Additionally, there is an atypical polar amino acid residue (Thr3.46) in both CB2 and CB1 compared with a conserved non-polar (I/L/M/V) residue in most (95%) class A GPCRs. Previous studies (D'Antona et al., 2006) and our own data (Hua et al., 2017) showed that T3.46A mutation disables CB2 or CB1 in coupling G$_i$ protein. Based on our receptor-G$_i$ complex structures, we found that upon activation in both CB2 or CB1, Tyr7.53 establishes new contacts with Thr3.46, Leu3.43, and Arg3.50 (Figures S5G and S5H). Meanwhile, Asp6.30 in TM6 interrupts its salt-bridge interaction with Arg3.50 (Figure S3D). This strengthens the interaction of TM3 and TM7, weakens the constraint on TM6 from TM3, and unlocks the outward movement of TM6. Therefore, T3.46A mutation in cannabinoid receptors or some other class A GPCRs may lead to restriction of the movement of TM6 and inactivation of the receptor.

Furthermore, previous studies have shown that a contact between residues 2.42 and 3.46 is important for GPCR folding (Venkatakrishnan et al., 2013). In CB2, the side chain of Phe72$^{2.42}$ adopts similar rotamer conformations in all three states, and the contacts between TM2 and TM3 are maintained. However, in CB1, the side chain of Phe155$^{2.42}$ adopts different conformations in the three states, which facilitate the conformational flexibility of ICL1 and the cytoplasmic end of TM2. This feature may indicate that these regions in CB1 may potentially be allosteric modulation sites. Of note, the cholesterol that we
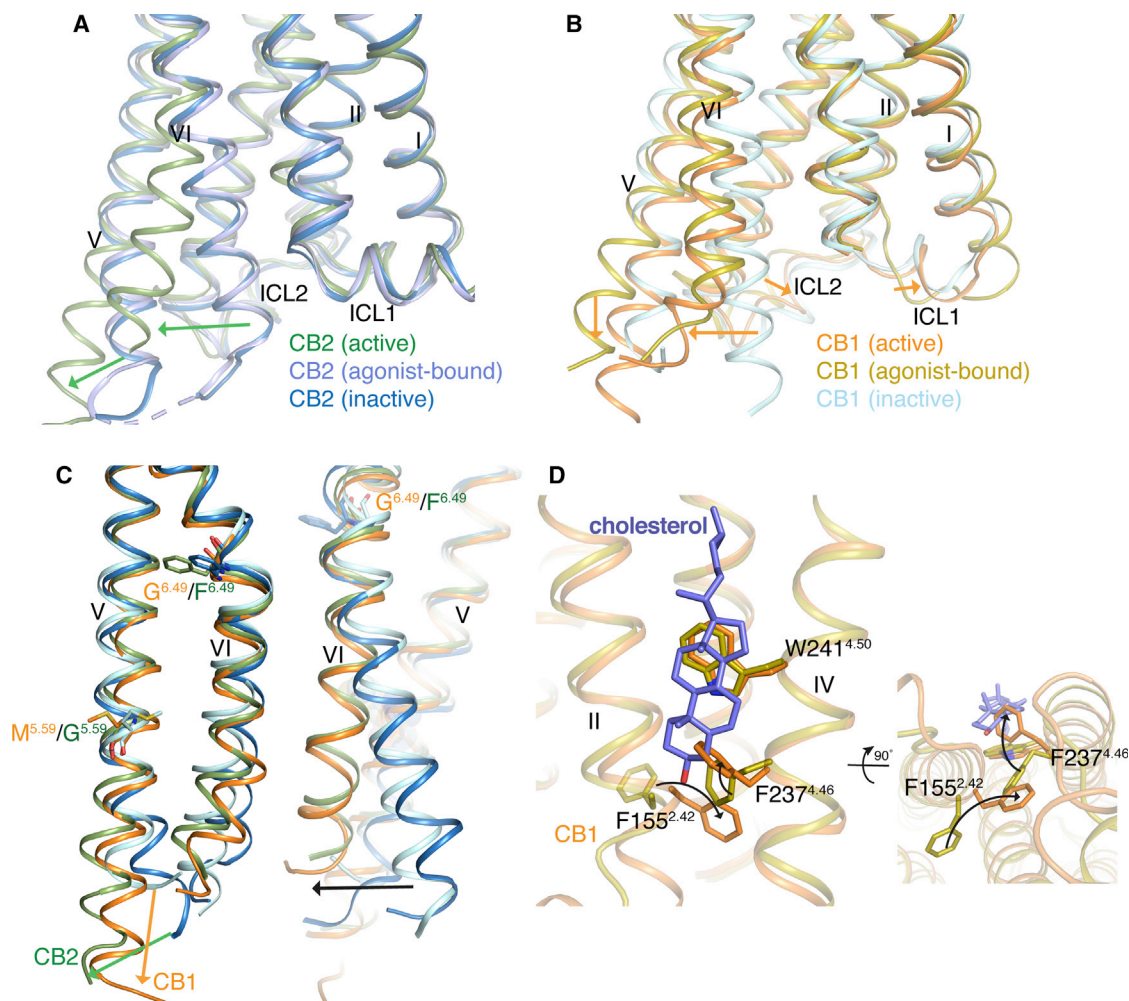
Figure 5. Comparison of CB1 and CB2 in Different States
(A) Comparison of the intracellular parts of CB2 in different states. Color code is as follows: CB2-Gi, green; CB2-AM12033, light blue; and CB2-AM10257, blue.
(B) Comparison of the intracellular parts of CB1 in different states. Color code is as follows: CB1-G$_i$, orange; CB1-AM841, olive; and CB1-AM6538, cyan.
(C) Conformation comparison of TM5 and TM6 in CB1 and CB2 between inactive and active states with color code as above.
(D) Conformational changes of F155$^{2.42}$ and F237$^{4.46}$ in cholesterol, slate sticks, binding sites of CB1.
See also Figure S5.

observed in the agonists-bound (AM11542 and AM841) CB1 crystal structures disappeared in the CB1-G$_i$ complex structure. Comparing with the cholesterol-binding pocket in agonist AM841 or AM11542 bound structures, the side chains of Phe155$^{2.42}$ and Phe237$^{4.46}$ undergo large conformational changes in CB1-G$_i$ structure and occupy the same position that cholesterol had in the agonist-bound crystal structures (Figure 5D). Also, the key residues involved in cholesterol binding are not conserved in CB1 and CB2. To our knowledge, Phe4.46 is unique to CB1 in class A GPCRs, and the cholesterol is not observed in either state of CB2 complex structures.

Structural Basis and Implications of CB1 and CB2 Agonist Selectivity

The structures we obtained so far reveal the similarity and diversity of antagonist- and agonist-binding modes in CB1 and CB2.

The antagonist-binding pockets in both receptors are quite distinct, which is consistent with their high degree of antagonist selectivity (Hua et al., 2016; Li et al., 2019). However, the agonist-binding pockets in CB1 and CB2 and even the side-chain rotamers of the key residues involved with ligands interactions are almost identical (Figure 6A). Such structural observations may explain the low level of CB1 and CB2 selectivity found in the classical cannabinoids and their synthetic analogs.

In this study, to further explore the structural basis of agonist selectivity in CB1 and CB2, two highly CB2-selective agonists, HU-308 and L-759,656, were chosen as model ligands to probe the problems. The binding affinity of HU-308 for CB2 (K_i is 22.7 nM) is about 5,000 times higher than that of CB1 (almost no measurable K_i) (Hanus et al., 1999), while L-759,656 shows a binding affinity more than 406 times higher on CB2 (K_i is 11.8 nM) than that of CB1 (K_i is 4.8 μM) (Ross et al., 1999). The
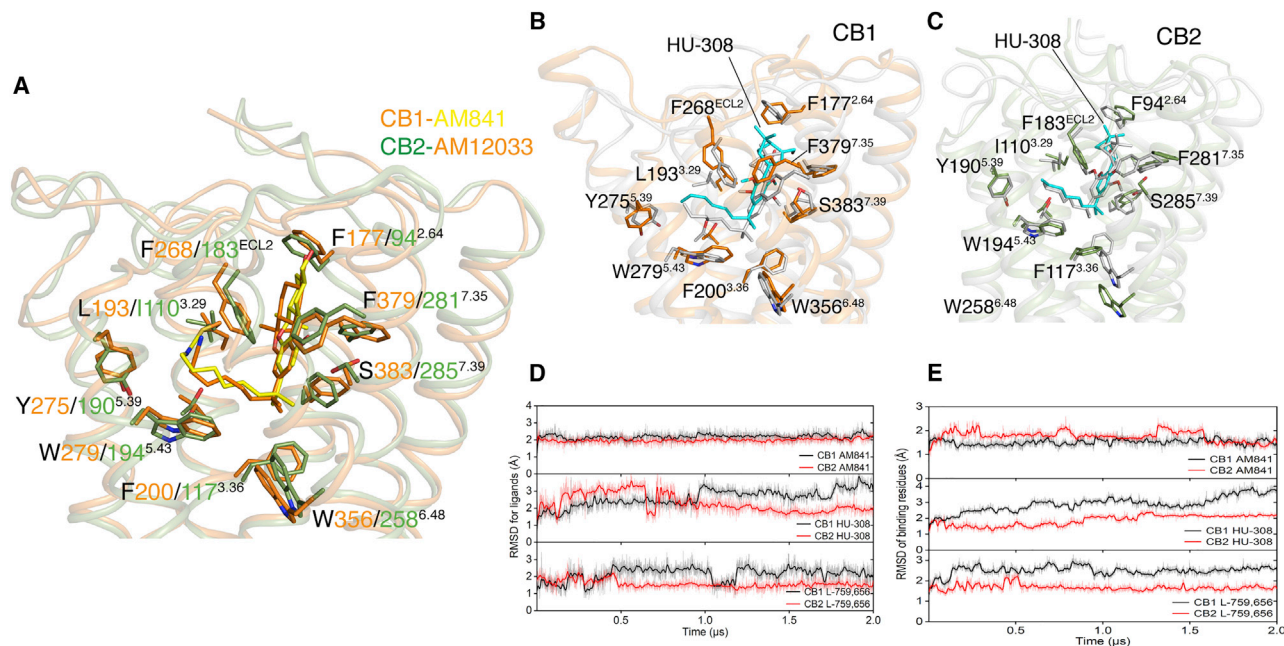
Figure 6. Docking Poses of HU-308 in CB1 and CB2 and MD Simulations

(A) Binding pocket comparison of AM841-bound CB1-G$_i$ complex and AM12033-bound CB2-G$_i$ complex.

(B) The initial docking pose of HU-308, gray sticks, in CB1, gray cartoon. After 2 μs MD simulation, HU-308 is shown as cyan sticks and CB1 is shown as orange cartoon.

(C) The initial docking pose of HU-308, gray sticks, in CB2, gray cartoon. After 2 μs MD simulation, HU-308 is shown as cyan sticks and CB2 is shown as green cartoon.

(D) RMSD of AM841, HU-308, and L-759,656 in CB1 or CB2 during 2 μs MD simulation.

(E) RMSD of key residues involved in the binding of AM841, HU-308, or L-759,656 in CB1 or CB2 during 2 μs MD simulation.

See also Figure S5.

ligand binding to a target protein is a dynamic process which involves synergetic conformational changes of both protein and ligand. Thus, we decided to employ the molecular dynamic (MD) simulations and meta dynamics (metaMD) simulations to study the ligand-binding process into CB1 and CB2 structures (Figures 6B, 6C, S5I, and S5J) (Barducci et al., 2011, 2008). For quality-control purpose, the non-selective agonists AM841 and AM12033 were used as positive controls.

In order to characterize the different binding processes of HU-308, L-759,656 and AM841 in CB1 and CB2, we calculated the RMSDs of ligands (RMSD$_{ligand}$) and key residues which are involved with ligand binding (RMSD$_{molecule}$) during each simulation course. The calculation results are shown in Figures 6D and 6E. The RMSD values represent the conformation fluctuations for ligands or key residues during the 2 μs simulation process. Thus, the smaller RMSD value denotes more stable ligand-receptor binding. Not surprisingly, the RMSD$_{AM841}$ in both CB1 and CB2, RMSD$_{CB1}$, and RMSD$_{CB2}$ all kept almost constant similar values (Figures 6D and 6E). These results indicate that our evaluation strategy is valid. Fortunately, the RMSD values for HU-308 or L-759,656 in CB1 are obviously larger than those of CB2. Similarly, the RMSD values for key residues in HU-308- or L-759,656-bound CB1 are clearly bigger than those of CB2 (Figures 6D and 6E). Therefore, the MD simulation results agree with the different ligand-binding affinities with CB1 and CB2.

To dig further into the understanding of the principle of agonist selectivity in CB1 and CB2, we introduced an advanced free energy sampling method, the well-tempered metaMD simulations

(Barducci et al., 2011, 2008), to sample ligand-binding paths. MetaMD is a reliable method and has been widely used for many rare biological event samplings (Barducci et al., 2011; Bonomi et al., 2009; Yuan et al., 2014). Since the N termini in both CB1 and CB2 cover the orthosteric sites, the ligand entry process may be influenced. Thus, we selected two collective variables for our simulations: distance between the mass center of a ligand and that of the binding pocket and distance between the mass center of N terminus and that of ECL2 loop.

In the case of HU-308, the binding processes are composed of three different stages in both CB1 and CB2 (Figure 7). Initially, HU-308 fluctuated in the bulk environment at the extracellular region in the vicinity of position P1. At a certain stage, the N terminus overcame energy barriers and opened an empty space to accommodate initial ligand binding. The free energy surface (FES) plot indicated that the energy barriers were similar for CB1 and CB2, i.e., approximately 3.5 kcal/mol and 3.0 kcal/mol, respectively. However, when HU-308 diffused into a deeper space toward the orthosteric site, the energy barrier increased noticeably. It was about 10.5 kcal/mol for CB1, whereas it was about 5.0 kcal/mol for CB2 (Figures 7C and 7D). Such an obvious difference should explain why HU-308 is much more potent against CB2.

DISCUSSION

In this study, we compared and analyzed the structure snapshots of CB2 and CB1 in their inactive, active-like, and activated
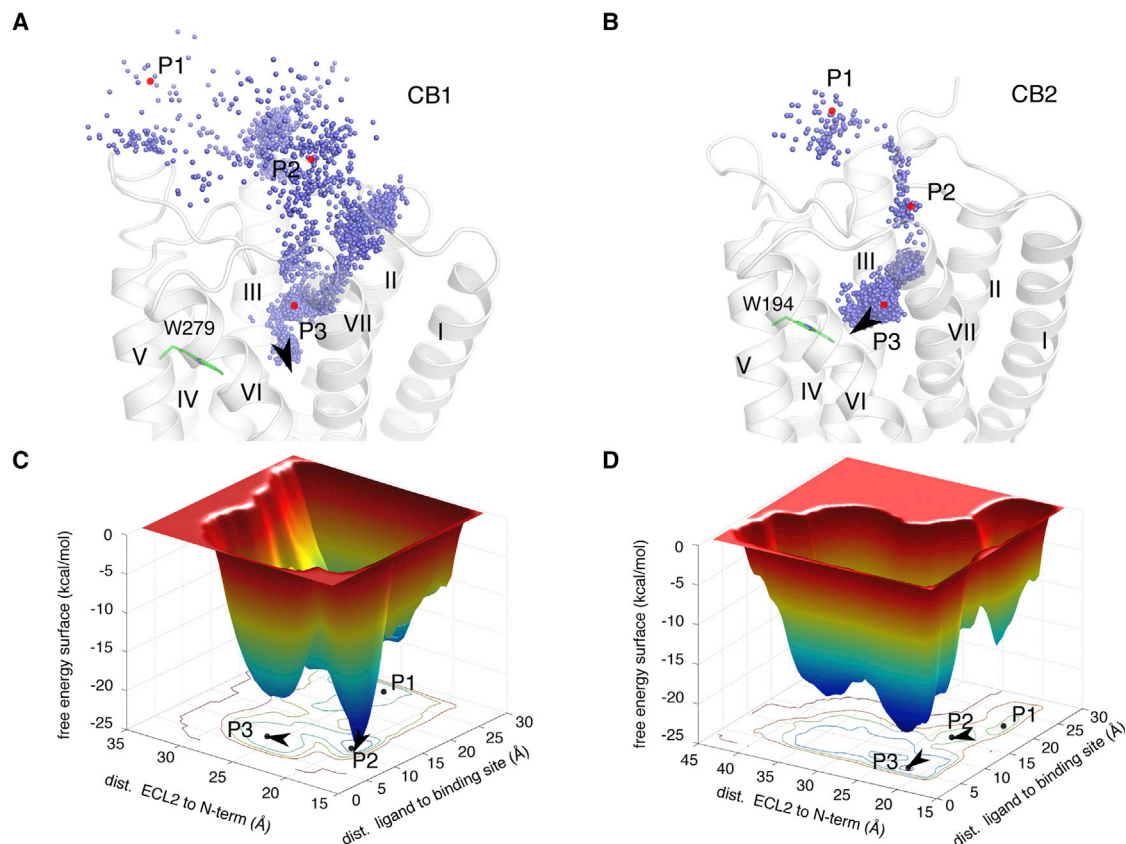
Figure 7. MetaMD Simulations of HU-308 in CB1 and CB2

(A) The mass center, blue sphere, of HU-308 in metaMD simulation against CB1. Three typical positions P1-P3 were labeled in red. P1: bulk environment in the extracellular region. P2: initial ligand-binding position when N-terminal opened. P3: fully ligand-binding position in the orthosteric site.

(B) The mass center, blue sphere of HU-308 in metaMD simulation against CB2. Three typical positions P1-P3 are labeled in red.

(C and D) The free energy surface (FES) of metaMD simulations for systems CB1-HU-308 (C) and for that of CB2-HU-308 (D).

See also Videos S1 and S2.

signaling states and deciphered their activation and signaling mechanism. Although the overall architecture is similar between CB2-AM12033-G$_i$ and CB1-AM841-G$_i$, CB2 and CB1 exhibit distinct characters in terms of ligand and G protein selectivity and activation process. The single reside difference in ICL2 (L222 in CB1 and P139 in CB2) may contribute to the G protein-coupling diversity of cannabinoid receptors, where CB2 is specific to G$_i$ only while CB1 can couple with G$_i$, G$_s$, and G$_q$. The high degree of structural similarity in the orthosteric binding pockets between agonist-bound CB2 and CB1 imposes substantial challenges for high-selective agonist design. The MD and metaMD simulation analysis on the selectivity of HU-308 and L-759,656 implied the possible connection between agonist selectivity and agonist entry path into CB2 or CB1.

The other interesting finding of this study is the cholesterol-binding behavior with CB1. Our collective experimental evidence encourages us to speculate that cholesterol or other steroids may be the endogenous allosteric modulator of CB1. This idea is supported by previous data which showed that pregnenolone, a derivative of cholesterol, acts as a CB1 allosteric modulator (Vallée et al., 2014). We believe that pregnenolone may also

bind to the same cholesterol-binding region in CB1 owing to their similar structural scaffolds. In summary, our findings uncovered new clues in understanding the activation and signaling mechanism of cannabinoid receptors and will help the precise modulation of endocannabinoid systems for therapeutic benefit.

STAR★METHODS

Detailed methods are provided in the online version of this paper and include the following:

- KEY RESOURCES TABLE
- LEAD CONTACT AND MATERIALS AVAILABILITY
- EXPERIMENTAL MODEL AND SUBJECT DETAILS
  - Cell lines
- METHOD DETAILS
  - Synthesis and Characterization of AM12033
  - Protein Engineering and Expression of CB2 for Crystallography Study
  - CB2-AM12033 Complex Purification for Co-crystallization

SUPPLEMENTAL INFORMATION

Supplemental Information can be found online at https://doi.org/10.1016/j.cell.2020.01.008.

AUTHOR CONTRIBUTIONS

Conceptualization, T.H., A.M., and Z.-J.L.; Methodology, T.H., X.L., L.W., C.I.T., Y.W., L.S., C.A.J., S.P.N., X.S., Q.S., S.J., T.W.G., O.B., E.L.S., and N.Z.; Validation, M.W., Y.W., L.W., and F.S.; Formal Analysis, T.H., X.L., S.Y., S.Z., L.M.B., A.M., and Z.-J.L.; Investigation, T.H. and X.L.; Writing – Original Draft, T.H. and X.L.; Writing – Review & Editing, T.H., X.L., S.P.N., M.W., S.Y., S.Z., L.M.B., A.M., and Z.-J.L.; Visualization, T.H., X.L., S.P.N., and M.W.; Supervision, A.M. and Z.-J.L.

DECLARATION OF INTERESTS

The authors declare no competing interests.

REFERENCES

Abraham, M.J., Murtola, T., Schulz, R., Páll, S., Smith, J.C., Hess, B., and Lindahl, E. (2015). GROMACS: High performance molecular simulations through multi-level parallelism from laptops to supercomputers. SoftwareX, 1–2, 19–25.

Adams, P.D., Afonine, P.V., Bunkóczi, G., Chen, V.B., Davis, I.W., Echols, N., Headd, J.J., Hung, L.W., Kapral, G.J., Grosse-Kunstleve, R.W., et al. (2010). PHENIX: a comprehensive Python-based system for macromolecular structure solution. Acta Crystallogr. D Biol. Crystallogr. 66, 213–221.

Ballesteros, J.A., and Weinstein, H. (1995). Integrated methods for the construction of three-dimensional models and computational probing of structure-function relations in G protein-coupled receptors. Methods in Neurosciences 25, 366–428.

Barducci, A., Bussi, G., and Parrinello, M. (2008). Well-tempered metadynamics: a smoothly converging and tunable free-energy method. Phys. Rev. Lett. 100, 020603.

Barducci, A., Bonomi, M., and Parrinello, M. (2011). Metadynamics. WIREs Comput. Mol. Sci. 1, 826–843.

Bonomi, M., Barducci, A., and Parrinello, M. (2009). Reconstructing the equilibrium Boltzmann distribution from well-tempered metadynamics. J. Comput. Chem. 30, 1615–1621.

Caffrey, M., and Cherezov, V. (2009). Crystallizing membrane proteins using lipidic mesophases. Nat. Protoc. 4, 706–731.

Chan, H.C.S., Wang, J., Palczewski, K., Filipek, S., Vogel, H., Liu, Z.J., and Yuan, S. (2018). Exploring a new ligand binding site of G protein-coupled receptors. Chem. Sci. (Camb.) 9, 6480–6489.

Chen, V.B., Arendall, W.B., 3rd, Headd, J.J., Keedy, D.A., Immormino, R.M., Kapral, G.J., Murray, L.W., Richardson, J.S., and Richardson, D.C. (2010a). MolProbity: all-atom structure validation for macromolecular crystallography. Acta Crystallogr. D Biol. Crystallogr. 66, 12–21.

Chen, X.P., Yang, W., Fan, Y., Luo, J.S., Hong, K., Wang, Z., Yan, J.F., Chen, X., Lu, J.X., Benovic, J.L., and Zhou, N.M. (2010b). Structural determinants in the second intracellular loop of the human cannabinoid CB1 receptor mediate selective coupling to G(s) and G(i). Br. J. Pharmacol. 161, 1817–1834.

Cherezov, V., Hanson, M.A., Griffith, M.T., Hilgart, M.C., Sanishvili, R., Nagarajan, V., Stepanov, S., Fischetti, R.F., Kuhn, P., and Stevens, R.C. (2009). Rastering strategy for screening and centring of microcrystal samples of human membrane proteins with a sub-10 microm size X-ray synchrotron beam. J. R. Soc. Interface 6 (Suppl 5), S587–S597.

Contino, M., Capparelli, E., Colabufo, N.A., and Bush, A.I. (2017). Editorial: The CB2 Cannabinoid System: A New Strategy in Neurodegenerative Disorder and Neuroinflammation. Front. Neurosci. 11, 196.

D'Antona, A.M., Ahn, K.H., and Kendall, D.A. (2006). Mutations of CB1 T210 produce active and inactive receptor forms: correlations with ligand affinity, receptor stability, and cellular localization. Biochemistry 45, 5606–5617.

Darden, T., York, D., and Pedersen, L. (1993). Particle mesh Ewald: An Nlog(N) method for Ewald sums in large systems. J. Chem. Phys. 98, 10089–10092.

Draper-Joyce, C.J., Khoshouei, M., Thal, D.M., Liang, Y.L., Nguyen, A.T.N., Furness, S.G.B., Venugopal, H., Baltos, J.A., Plitzko, J.M., Danev, R., et al. (2018). Structure of the adenosine-bound human adenosine A_1 receptor-G_i complex. Nature 558, 559–563.

Emsley, P., Lohkamp, B., Scott, W.G., and Cowtan, K. (2010). Features and development of Coot. Acta Crystallogr. D Biol. Crystallogr. 66, 486–501.

Erlandson, S.C., McMahon, C., and Kruse, A.C. (2018). Structural Basis for G Protein-Coupled Receptor Signaling. Annu. Rev. Biophys. Published online March 2, 2018. https://doi.org/10.1146/annurev-biophys-070317-032931.

Fernandez-Leiro, R., and Scheres, S.H.W. (2017). A pipeline approach to single-particle processing in RELION. Acta. Crystallogr. D. Struct. Biol. 73, 496–502.

Friesner, R.A., Banks, J.L., Murphy, R.B., Halgren, T.A., Klicic, J.J., Mainz, D.T., Repasky, M.P., Knoll, E.H., Shelley, M., Perry, J.K., et al. (2004). Glide: a new approach for rapid, accurate docking and scoring. 1. Method and assessment of docking accuracy. J. Med. Chem. 47, 1739–1749.

Friesner, R.A., Murphy, R.B., Repasky, M.P., Frye, L.L., Greenwood, J.R., Halgren, T.A., Sanschagrin, P.C., and Mainz, D.T. (2006). Extra precision glide: docking and scoring incorporating a model of hydrophobic enclosure for protein-ligand complexes. J. Med. Chem. *49*, 6177–6196.

García-Nafría, J., Nehmé, R., Edwards, P.C., and Tate, C.G. (2018). Cryo-EM structure of the serotonin 5-HT$_{1B}$ receptor coupled to heterotrimeric G$_o$. Nature *558*, 620–623.

Glass, M., and Felder, C.C. (1997). Concurrent stimulation of cannabinoid CB1 and dopamine D2 receptors augments cAMP accumulation in striatal neurons: evidence for a Gs linkage to the CB1 receptor. J. Neurosci. *17*, 5327–5333.

Grant, T., Rohou, A., and Grigorieff, N. (2018). cisTEM: user-friendly software for single-particle image processing. eLife *7*, e14874.

Guzmán, M. (2003). Cannabinoids: potential anticancer agents. Nat. Rev. Cancer *3*, 745–755.

Hanus, L., Breuer, A., Tchilibon, S., Shiloah, S., Goldenberg, D., Horowitz, M., Pertwee, R.G., Ross, R.A., Mechoulam, R., and Fride, E. (1999). HU-308: a specific agonist for CB(2), a peripheral cannabinoid receptor. Proc. Natl. Acad. Sci. USA *96*, 14228–14233.

Heymann, J.B. (2001). Bsoft: image and molecular processing in electron microscopy. J. Struct. Biol. *133*, 156–169.

Hua, T., Vemuri, K., Pu, M., Qu, L., Han, G.W., Wu, Y., Zhao, S., Shui, W., Li, S., Korde, A., et al. (2016). Crystal Structure of the Human Cannabinoid Receptor CB1. Cell *167*, 750–762.14.

Hua, T., Vemuri, K., Nikas, S.P., Laprairie, R.B., Wu, Y., Qu, L., Pu, M., Korde, A., Jiang, S., Ho, J.H., et al. (2017). Crystal structures of agonist-bound human cannabinoid receptor CB$_1$. Nature *547*, 468–471.

Huang, J., Rauscher, S., Nawrocki, G., Ran, T., Feig, M., de Groot, B.L., Grubmüller, H., and MacKerell, A.D., Jr. (2017). CHARMM36m: an improved force field for folded and intrinsically disordered proteins. Nat. Methods *14*, 71–73.

Jo, S., Kim, T., Iyer, V.G., and Im, W. (2008). CHARMM-GUI: a web-based graphical user interface for CHARMM. J. Comput. Chem. *29*, 1859–1865.

Kabsch, W. (2010). Integration, scaling, space-group assignment and post-refinement. Acta Crystallogr. D Biol. Crystallogr. *66*, 133–144.

Koehl, A., Hu, H., Maeda, S., Zhang, Y., Qu, Q., Paggi, J.M., Latorraca, N.R., Hilger, D., Dawson, R., Matile, H., et al. (2018). Structure of the μ-opioid receptor-G$_i$ protein complex. Nature *558*, 547–552.

Krishna Kumar, K., Shalev-Benami, M., Robertson, M.J., Hu, H., Banister, S.D., Hollingsworth, S.A., Latorraca, N.R., Kato, H.E., Hilger, D., Maeda, S., et al. (2019). Structure of a Signaling Cannabinoid Receptor 1-G Protein Complex. Cell *176*, 448–458.e12.

Lauckner, J.E., Hille, B., and Mackie, K. (2005). The cannabinoid agonist WIN55,212-2 increases intracellular calcium via CB1 receptor coupling to Gq/11 G proteins. Proc. Natl. Acad. Sci. USA *102*, 19144–19149.

Lemberger, L. (1980). Potential therapeutic usefulness of marijuana. Annu. Rev. Pharmacol. Toxicol. *20*, 151–172.

Li, X., Hua, T., Vemuri, K., Ho, J.H., Wu, Y., Wu, L., Popov, P., Benchama, O., Zvonok, N., Locke, K., et al. (2019). Crystal Structure of the Human Cannabinoid Receptor CB2. Cell *176*, 459–467.e13.

Liu, Y., Ji, L., Eno, M., Kudalkar, S., Li, A.L., Schimpgen, M., Benchama, O., Morales, P., Xu, S., Hurst, D., et al. (2018). (R)- N-(1-Methyl-2-hydroxyethyl)-13-(S)-methyl-arachidonamide (AMG315): A Novel Chiral Potent Endocannabinoid Ligand with Stability to Metabolizing Enzymes. J. Med. Chem. *61*, 8639–8657.

Lunn, C.A., Reich, E.P., Fine, J.S., Lavey, B., Kozlowski, J.A., Hipkin, R.W., Lundell, D.J., and Bober, L. (2008). Biology and therapeutic potential of cannabinoid CB2 receptor inverse agonists. Br. J. Pharmacol. *153*, 226–239.

Maeda, S., Qu, Q., Robertson, M.J., Skiniotis, G., and Kobilka, B.K. (2019). Structures of the M1 and M2 muscarinic acetylcholine receptor/G-protein complexes. Science *364*, 552–557.

Makriyannis, A., D'Souza, M.R., Sharma, R., Nikas, S.P., and Thakur, G.A. (2014). 2-cycloalkyl resorcinol cannabinergic ligands. Northeastern University patent application WO2014062965 A1, filed October 17, 2013, and published April 24, 2014.

Makriyannis, A., Nikas, S.P., Khanolkar, A., and Thakur, G.A. (2007). Methods of preparation and use of novel bicyclic cannabinoids. University of Connecticut patent application US20070135388 A1, filed December 12, 2006, and published June 14, 2007.

Mastronarde, D.N. (2005). Automated electron microscope tomography using robust prediction of specimen movements. J. Struct. Biol. *152*, 36–51.

McCoy, A.J., Grosse-Kunstleve, R.W., Adams, P.D., Winn, M.D., Storoni, L.C., and Read, R.J. (2007). Phaser crystallographic software. J. Appl. Cryst. *40*, 658–674.

Munro, S., Thomas, K.L., and Abu-Shaar, M. (1993). Molecular characterization of a peripheral receptor for cannabinoids. Nature *365*, 61–65.

Nikas, S.P., Thakur, G.A., Parrish, D., Alapafuja, S.O., Huestis, M.A., and Makriyannis, A. (2007). A concise methodology for the synthesis of (−)-Δ 9-tetrahydrocannabinol and (−)-Δ 9-tetrahydrocannabivarin metabolites and their regiospecifically deuterated analogs. Tetrahedron *63*, 8112–8123.

Nikas, S.P., Alapafuja, S.O., Papanastasiou, I., Paronis, C.A., Shukla, V.G., Papahatjis, D.P., Bowman, A.L., Halikhedkar, A., Han, X., and Makriyannis, A. (2010). Novel 1′,1′-chain substituted hexahydrocannabinols: 9β-hydroxy-3-(1-hexyl-cyclobut-1-yl)-hexahydrocannabinol (AM2389) a highly potent cannabinoid receptor 1 (CB1) agonist. J. Med. Chem. *53*, 6996–7010.

Nikas, S.P., Sharma, R., Paronis, C.A., Kulkarni, S., Thakur, G.A., Hurst, D., Wood, J.T., Gifford, R.S., Rajarshi, G., Liu, Y., et al. (2015). Probing the carboxyester side chain in controlled deactivation (-)-δ(8)-tetrahydrocannabinols. J. Med. Chem. *58*, 665–681.

Pettersen, E.F., Goddard, T.D., Huang, C.C., Couch, G.S., Greenblatt, D.M., Meng, E.C., and Ferrin, T.E. (2004). UCSF Chimera–a visualization system for exploratory research and analysis. J. Comput. Chem. *25*, 1605–1612.

Ranganathan, A., Dror, R.O., and Carlsson, J. (2014). Insights into the role of Asp79(2.50) in β2 adrenergic receptor activation from molecular dynamics simulations. Biochemistry *53*, 7283–7296.

Rohou, A., and Grigorieff, N. (2015). CTFFIND4: fast and accurate defocus estimation from electron micrographs. J. Struct. Biol. *192*, 216–221.

Ross, R.A., Brockie, H.C., Stevenson, L.A., Murphy, V.L., Templeton, F., Makriyannis, A., and Pertwee, R.G. (1999). Agonist-inverse agonist characterization at CB1 and CB2 cannabinoid receptors of L759633, L759656, and AM630. Br. J. Pharmacol. *126*, 665–672.

Ryckaert, J.P.C., Ciccotti, G., and Berendsen, H.J.C. (1977). Numerical integration of the cartesian equations of motion of a system with constrains: Molecular dynamics of n-alkanes. J. Comp. Physiol. *23*, 327–341.

Sastry, G.M., Adzhigirey, M., Day, T., Annabhimoju, R., and Sherman, W. (2013). Protein and ligand preparation: parameters, protocols, and influence on virtual screening enrichments. J. Comput. Aided Mol. Des. *27*, 221–234.

Savinainen, J.R., Saario, S.M., Niemi, R., Järvinen, T., and Laitinen, J.T. (2003). An optimized approach to study endocannabinoid signaling: evidence against constitutive activity of rat brain adenosine A1 and cannabinoid CB1 receptors. Br. J. Pharmacol. *140*, 1451–1459.

Scheres, S.H. (2012). RELION: implementation of a Bayesian approach to cryo-EM structure determination. J. Struct. Biol. *180*, 519–530.

Shao, Z., Yin, J., Chapman, K., Grzemska, M., Clark, L., Wang, J., and Rosenbaum, D.M. (2016). High-resolution crystal structure of the human CB1 cannabinoid receptor. Nature *540*, 602–606.

Sharma, R., Nikas, S.P., Paronis, C.A., Wood, J.T., Halikhedkar, A., Guo, J.J., Thakur, G.A., Kulkarni, S., Benchama, O., Raghav, J.G., et al. (2013).

Controlled-deactivation cannabinergic ligands. J. Med. Chem. *56*, 10142–10157.

Smart, O.S., Womack, T.O., Flensburg, C., Keller, P., Paciorek, W., Sharff, A., Vonrhein, C., and Bricogne, G. (2012). Exploiting structure similarity in refinement: automated NCS and target-structure restraints in BUSTER. Acta Crystallogr. D Biol. Crystallogr. *68*, 368–380.

Vallée, M., Vitiello, S., Bellocchio, L., Hébert-Chatelain, E., Monlezun, S., Martin-Garcia, E., Kasanetz, F., Baillie, G.L., Panin, F., Cathala, A., et al. (2014). Pregnenolone can protect the brain from cannabis intoxication. Science *343*, 94–98.

Venkatakrishnan, A.J., Deupi, X., Lebon, G., Tate, C.G., Schertler, G.F., and Babu, M.M. (2013). Molecular signatures of G-protein-coupled receptors. Nature *494*, 185–194.

Yuan, S., Filipek, S., Palczewski, K., and Vogel, H. (2014). Activation of G-protein-coupled receptors correlates with the formation of a continuous internal water pathway. Nat. Commun. *5*, 4733.

Yuan, S., Filipek, S., and Vogel, H. (2016). A Gating Mechanism of the Serotonin 5-HT3 Receptor. Structure *24*, 816–825.

Zhang, K. (2016). Gctf: Real-time CTF determination and correction. J. Struct. Biol. *193*, 1–12.

Zheng, C., Chen, L., Chen, X., He, X., Yang, J., Shi, Y., and Zhou, N. (2013). The second intracellular loop of the human cannabinoid CB2 receptor governs G protein coupling in coordination with the carboxyl terminal domain. PLoS ONE *8*, e63262.

Zheng, S.Q., Palovcak, E., Armache, J.P., Verba, K.A., Cheng, Y., and Agard, D.A. (2017). MotionCor2: anisotropic correction of beam-induced motion for improved cryo-electron microscopy. Nat. Methods *14*, 331–332.

Zoete, V., Cuendet, M.A., Grosdidier, A., and Michielin, O. (2011). SwissParam: a fast force field generation tool for small organic molecules. J. Comput. Chem. *32*, 2,359–2,368.

STAR★METHODS

KEY RESOURCES TABLE

REAGENT or RESOURCE	SOURCE	IDENTIFIER
Chemicals, Peptides, and Recombinant Proteins		
EDTA-free complete protease inhibitor cocktail tablets	Roche	Cat#5056489001
Iodoacetamide	Sigma	Cat#I1149
Lauryl Maltose Neopentyl Glycerol (LMNG)	Anatrace	Cat#4216588
Cholesterol hemisucinate (CHS)	Sigma	Cat#C6512
TCEP	Thermo Fisher Scientific	Cat#77720
Apyrase	New England Biolabs	Cat#M0398S
GDN (glycol-diosgenin): Synthetic Digitonin Substitute	Anatrace	Cat#GDN101
Ethylenediamine Tetraacetic Acid (EDTA)	Fisher Scientific	Cat#S311-500
N-[4-(7-diethylamino-4-methyl-3-coumarinyl)phenyl]maleimide (CPM)	Invitrogen	Cat#D10251
TALON IMAC resin	Clontech	Cat#635507
1-Oleoyl-rac-glycerol (monoolein)	Sigma	Cat#M7765
Magnesium Chloride	Fisher Scientific	Cat#BP214-500
Protein Assay Dye	Biorad	5000006
Cholesterol	Sigma	Cat#C8667
CP55,940	Tocris	Cat#0949
AM12033	This paper	N/A
AM841	This paper	N/A
[³H]CP55,940	NIDA Drug Supply Program	NOCD-092
SR144528	NIDA Drug Supply Program	NOCD-085
4-methyl-5-phenyl-1*H*-pyrazole-3-carboxylic acid	ChemBridge	4036397
1-adamantylamine	Sigma-Aldrich	138576
O-(benzotriazol-1-yl)-*N,N,N',N'*-tetramethyluronium tetrafluoroborate	Sigma-Aldrich	12806
Hünig's base	Sigma-Aldrich	D125806
Sodium Hydride	Sigma-Aldrich	452912
5-Bromo-1-pentanol	Sigma-Aldrich	670855
N,N-Dimethylformamide	Sigma-Aldrich	227056
dichloromethane	Sigma-Aldrich	D65100
sodium sulfate	Sigma-Aldrich	239313
silica gel columns	Biotage	FSUL-0442
Critical Commercial Assays		
HTRF HiRange cAMP Assay Kit	CISBIO	Cat# 62AM6PEC
PathHunter Detection Kit	DiscoveRx	Cat#93-0001
Q5 site directed mutagenesis kit	NEB	Cat#E0554S
In-Fusion® HD EcoDry™ Cloning System	Clontech	Cat#639684
Deposited Data		
CB2_AM12033 complex structure	This paper	PDB: 6KPC
CB2-Gi EM map	This paper	PDB: 6KPF
CB1-Gi EM map	This paper	PDB: 6KPG

Continued

REAGENT or RESOURCE	SOURCE	IDENTIFIER
Experimental Models: Cell Lines		
Spodoptera frugiperda (Sf9)	Expression Systems	N/A
HEK293F human cell line	Expression Systems	CRL-1573
Primers for Site-Direct Mutagenesis		
G78L_forward:TTGGCTCTGGCTGACTTC	This paper	N/A
G78L_reverse:GCTGCCAATGAACAGGTATG	This paper	N/A
T127A_forward:GCTGGCCGCCATTGA	This paper	N/A
T127A_reverse:AGGAGGCTACCCACAGA	This paper	N/A
T153L_forward:GGTGCTCCTGGGCATC	This paper	N/A
T153L_reverse:AGTGCCCTTCCACGG	This paper	N/A
G210A_forward: ATCATCTACACCTATGCCCAC GTGCTCTGGAAG	This paper	N/A
G210A_reverse: CTTCCAGAGCACGTGGGCATA GGTGTAGATGAT	This paper	N/A
R242E_forward:GATGTGGAGTTGGCCAAGAC	This paper	N/A
R242E_reverse:CAGCCTCATTCGGGCC	This paper	N/A
G304E_forward:GAGTGAAGAGATCCGCTCC	This paper	N/A
G304E_reverse:CGTAGAGCATAGATGACAGGG	This paper	N/A
Recombinant DNA		
pFastBac1-CB2	This paper	N/A
pTT5-CB1	This paper	N/A
pFastBac1-Gα	This paper	N/A
pFastBacDual-G$\beta\gamma$	This paper	N/A
pFastBac1-scFv16	This paper	N/A
Software and Algorithms		
Schrödinger Suite 2015-4	Schrödinger	https://www.schrodinger.com
GROMACS 5.1.2	Abraham et al., 2015	www.gromacs.org
SwissParam	Zoete et al., 2011	www.swissparam.ch
XDS	Kabsch, 2010	Xds.mpimf-heidelberg.mpg.de
SCALA		www.ccp4.ac.uk/html/scala.html
Phaser	McCoy et al., 2007	www.phenix-online.org
Phenix	Adams et al., 2010	www.phenix-online.org
Buster	Smart et al., 2012	www.globalphasing.com/buster
COOT	Emsley et al., 2010	https://www2.mrc-lmb.cam.ac.uk/personal/pemsley/coot
SerialEM	Mastronarde, 2005	http://bio3d.colorado.edu/SerialEM/
MotionCor2	Zheng et al., 2017	https://emcore.ucsf.edu/ucsf-motioncor2
CTFFIND4	Rohou and Grigorieff, 2015	https://grigoriefflab.janelia.org/ctffind4
Relion	Fernandez-Leiro and Scheres, 2017	https://www2.mrc-lmb.cam.ac.uk/relion/index.php?title = Download_&_install
CisTEM	Grant et al., 2018	https://cistem.org/
Prism v.7.0	GraphPad Software	N/A
Other		
Solid white 384-well assay plates	VWR	Cat#82051-278 (CS)
Low-volume (20 μL) 384-well assay plates	VWR	Cat#784080
DMEM/F-12 (1:1) cell culture media	Invitrogen	Cat#11330-057

Continued

REAGENT or RESOURCE	SOURCE	IDENTIFIER
Opti-MEM cell culture media	Invitrogen	Cat#11058-021
FreeStyle™ 293 Expression Medium	Life Technologies	Cat#12338-026
DMEM	Invitrogen	Cat#11965-118
MEM	Invitrogen	Cat#11095-098
Phoenix package system	Stanford University	N/A
Penicillin/Streptomycin	Invitrogen	Cat#15140-122
Puromycin	Invitrogen	Cat#A11138-03
Hygromycin B	Life Technologies	Cat#10687-010
Geneticin	Life Technologies	Cat#10131-035
Bovine Serum Albumin, Fraction V, Cold-ethanol Precipitated	Fisher Scientific	Cat#BP1605100
Trypsin 0.5% EDTA	Invitrogen	Cat#25300-120
Dulbecco's phosphate-buffered saline (DPBS)	Invitrogen	Cat#14190250
4',6-Diamidino-2-phenylindole dihydrochloride (DAPI)	Sigma	Cat#D8417
Fetal Bovine Serum (FBS)	Life Technologies	Cat#16140089
Glass bottom dishes-uncoated (confocal plates)	MatTek	Cat#P35G-10-14-C
Collagen I	Fisher	Cat#CB40231
100kDa cutoff concentrators	Sartorius	Cat#VS0642
PD Minitrap G-25 coulmn	GE Healthcare	Cat#28-9180-07
96-well glass sandwich plates for LCP crystallization	NOVA	Cat#NOA90020
Lipofectamine® 2000	Thermo Scientific	11668027
96-well white microplate with bonded GF/B filter	PerkinElmer	Cat#6005177
500 cm^2 Square Cell Culture Dish	Corning	Cat#431110

LEAD CONTACT AND MATERIALS AVAILABILITY

Further information and requests for reagents may be directed to, and will be fulfilled by the Lead Contact, Zhi-Jie Liu (liuzhj@ shanghaitech.edu.cn). All unique/stable reagents generated in this study will be made available on request but we may require a payment and a completed Materials Transfer Agreement if there is potential for commercial application.

EXPERIMENTAL MODEL AND SUBJECT DETAILS

Cell lines
Spodoptera frugiperda (Sf9) cells were used for CB2 expression, crystallization, and co-expression of G protein for cryo-EM study. Sf9 cells were grown in ESF 921 medium (Expression systems) at 27°C and 125 rpm. Binding and functional experiments were performed with either CHO-K1 cell lines (ATCC, female) or U2OS cell lines (PathHunter EA Parental Cell lines, female, DiscoveRx). CHO-K1 cells were maintained in DMEM/F12 media supplemented with 10% fetal bovine serum (FBS), 1% penicillin/streptomycin, and 5 mg/mL puromycin for stable cell line selection (Invitrogen, Waltham, MA). U2OS cells were selected by geneticin selection (500 mg/mL) in MEM media supplemented with 10% FBS, 1% penicillin/streptomycin and 250 mg/mL hygromycin.

METHOD DETAILS

Synthesis and Characterization of AM12033
All reagents and solvents were purchased from Sigma-Aldrich Chemicals company, unless otherwise specified, and used without further purification. All anhydrous reactions were performed under a static argon atmosphere in flame-dried glassware using scrupulously dry solvents. Flash column chromatography employed silica gel 60 (230-400 mesh). All compounds were demonstrated to be homogeneous by analytical TLC on pre-coated silica gel TLC plates (Merck, 60 F$_{245}$ on glass, layer thickness 250 μm), and chromatograms were visualized by phosphomolybdic acid staining. Melting points were determined on a micro-melting point apparatus and are uncorrected. IR spectra were recorded on a Perkin Elmer Spectrum One FT-IR spectrometer. Peak strength is indicated as br (broad), w (weak), and s (strong). NMR spectra were recorded in CDCl$_3$, unless otherwise stated, on a Bruker Ultra Shield 400 WB plus (^{1}H at 400 MHz, ^{13}C at 100 MHz) or on a Varian INOVA-500 (^{1}H at 500 MHz, ^{13}C at 125 MHz) spectrometers and chemical shifts are reported in units of δ relative to internal TMS. Multiplicities are indicated as br (broadened), s (singlet), d (doublet), t (triplet), q (quartet),

qt (quintet) or m (multiplet). Coupling constants (J) are reported in hertz (Hz). Low and high-resolution mass spectra were performed in School of Chemical Sciences, University of Illinois at Urbana-Champaign. Mass spectral data are reported in the form of *m/z* (intensity relative to base = 100). LC/MS analysis was performed by using a Waters MicroMass ZQ system [electrospray-ionization (ESI) with Waters-2525 binary gradient module coupled to a Photodiode Array Detector (Waters-2996) and ELS detector (Waters-2424) using a XTerra MS C18, 5 μm, 4.6 mm x 50 mm column and acetonitrile/water].

**2-(3,5-Dimethoxyphenyl)-2-methylpropanenitrile (2) (Sharma et al., 2013)**
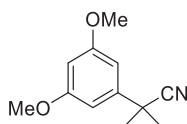
To a stirred suspension of sodium hydride (3.09 g, 128.6 mmol) in dry DMF (80 mL) at 0°C under an argon atmosphere was added dropwise a mixture of **1** (7.08 g, 40.0 mmol) and iodomethane (8.0 mL, 128.6 mmol) in dry DMF (4.2 mL). The reaction temperature was rose to 25°C over a 15 min period and stirring was continued for 2 h. The reaction mixture was quenched with saturated aqueous NH$_4$Cl solution and diluted with diethyl ether. The organic layer was separated and the aqueous layer was extracted with diethyl ether. The combined organic layer was washed with water and brine, dried (MgSO$_4$), and concentrated in vacuo. Purification by flash column chromatography on silica gel (25% ethyl acetate in hexane) gave the title compound (7.86 g, 96% yield) as a colorless oil. IR (neat) 2950, 2840, 2234 (w, CN), 1532, 1438, 1319, 1204, 788 cm^{-1}. ^{1}H NMR (500 MHz, CDCl$_3$) δ 6.61 (d, J = 2.0 Hz, 2H, Ar-H), 6.40 (t, J = 2.0 Hz, 1 H, Ar-H), 3.81 (s, 6 H, -OCH$_3$), 1.71 (s, 6 H, -C(CH$_3$)$_2$-); Mass spectrum (ESI) *m/z* (relative intensity) 206 (M$^+$+H, 100).

2-(3,5-Dimethoxyphenyl)-2-methylpropanal (3)(Nikas et al., 2015)
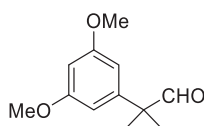
To a stirred solution of **2** (6.46 g, 31.5 mmol) in anhydrous CH$_2$Cl$_2$ (220 mL) at –78°C, under an argon atmosphere was added 1 M solution of DIBAL-H in Hexane (94 mL) dropwise and the reaction mixture was stirred for additional 30 min. The reaction mixture was then quenched by dropwise addition of potassium sodium tartrate (10% w/w solution in water) at – 78°C. Following the addition, the mixture was warmed to room temperature, stirred for an additional 50 min and then diluted with ethyl acetate. The organic phase was separated, and the aqueous phase was extracted with ethyl acetate. The combined organic layer was washed with brine, dried (MgSO$_4$), and the solvent was evaporated under reduced pressure. The crude product was purified by flash chromatography on silica gel (10%–35% ethyl acetate in hexane) to give 6.03 g of **3** as colorless oil in 92% yield. IR (neat) 2938, 2838, 2705 (w, CHO), 1725 (s, > C = O), 1595, 1457, 1424, 1314, 1205, 1156, 1066, 835 cm^{-1}. ^{1}H NMR (500 MHz, CDCl$_3$) δ 9.46 (s, 1H, -CHO), 6.40 (d, J = 2.0 Hz, 2H, 2-H, 6-H), 6.39 (t, J = 2.0 Hz, 1H, 4-H), 3.78 (s, 6H, -OMe), 1.43 (s, 6H, -C(CH$_3$)$_2$-). ^{13}C NMR (100 MHz CDCl$_3$) δ 201.6 (-CHO), 161.1 (ArC), 143.6 (ArC), 105.1 (ArC), 98.6 (ArC), 65.7 (> (C)CHO), 55.2 (-OCH$_3$), 50.5, 22.3. Mass spectrum (EI) m/z (relative intensity) 208 (M$^+$, 25), 196 (16), 179 (M$^+$-CHO), 165 (25), 151 (14), 139 (39), 91 (20), 77 (20). Exact mass (EI) calculated for C$_{12}$H$_{16}$O$_3$ (M$^+$), 208.10995; found, 208.11077.

(Z)-1,3-Dimethoxy-5-(2-methyl-7-phenoxyhept-3-en-2-yl)benzene (4)(Makriyannis et al., 2014)
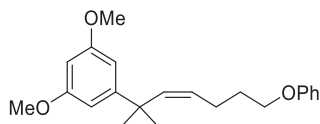
To a stirred suspension of (4-phenoxybutyl)triphenylphosphonium bromide (**15**)(Nikas et al., 2010) (43.32 g, 88.4 mmol) in dry THF (540 mL) at 0°C, under an argon atmosphere was added potassium bis(trimethylsilyl)amide (17.40 g, 87.1 mmol). The mixture was stirred for 30 min at 10°C to ensure complete formation of the orange phosphorane. A solution of aldehyde **3** (6.82 g, 32.8 mmol) in 8.6 mL THF was added dropwise to the resulting slurry, at 0°C. The reaction was stirred for 20 min at room temperature and upon completion was quenched by the addition of saturated aqueous NH$_4$Cl solution. The organic layer was separated and the aqueous phase was extracted with diethyl ether. The combined organic layer was washed with brine and dried (MgSO$_4$) and the solvent was evaporated under reduced pressure. The residue was purified on a silica gel (5%–15% diethyl ether in hexanes) to give 10.68 g of compound **4** as colorless oil in 96% yield. IR (neat) 2960, 2836, 1595, 1422, 1244, 1204, 1153, 1051, 753, 692 cm^{-1}. ^{1}H NMR (500 MHz, CDCl$_3$) δ 7.29-7.21 (m, 2H, 3-H, 5-H of -OPh), 6.91 (t, J = 7.3 Hz, 1H, 4-H of -OPh), 6.81 (d, J = 7.3 Hz, 2H, 2-H, 6-H of -OPh), 6.56 (d, J = 2.2 Hz, 2H, 2-H, 6-H), 6.28 (t, J = 2.2 Hz, 1H, 4-H), 5.69 (dt, J = 11.4, 1.7 Hz, 1H, 2'-H), 5.31 (dt, J = 11.4, 7.4 Hz, 1H, 3'-H), 3.77 (s, 6H, -OMe), 3.69 (t, J = 6.7 Hz, 2H, 6'-H), 1.83 (qd, J = 7.4, 1.7 Hz, 2H, 4'-H), 1.63 (qt, J = 7.0 Hz,

2H, 5′-H), 1.40 (s, 6H, -C(CH$_3$)$_2$-). ^{13}C NMR (100 MHz CDCl$_3$) δ 160.6 (ArC), 159.1 (ArC), 153.3 (ArC), 140.4 (> C = C <), 130.3 (> C = C <), 129.4 (ArC), 120.5 (ArC), 114.6 (ArC), 105.0 (ArC), 97.0 (ArC), 67.3 (C-6′), 55.3 (-OCH$_3$), 40.4, 31.4, 29.0, 24.9. Mass spectrum (ESI) *m/z* (relative intensity) 341 (M$^+$+H, 100), 247 (M$^+$+H-OPh, 30). LC/MS analysis (Waters MicroMass ZQ system) showed retention time of 5.6 min for the title compound.

### *1,3-Dimethoxy-5-(2-methyl-7-phenoxyheptan-2-yl)benzene (5)(Makriyannis et al., 2014)*
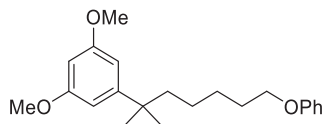
To a solution of **4** (6.85 g, 20.2 mmol) in ethyl acetate (200 mL) was added 10% w/w Pd/C (690 mg) and the resulting suspension stirred vigorously for 2.5 h under hydrogen atmosphere at room temperature. The catalyst was removed by filtration through celite, and the filtrate was evaporated under reduced pressure to afford 6.77 g of the crude product **5** as colorless oil, in 98% yield which was used in the next step without further purification. IR (neat) 2936, 2861, 1598, 1497, 1457, 1422, 1244, 1204, 1155, 1053, 832, 754, 692 cm^{-1}. ^{1}H NMR (400 MHz, CDCl$_3$) δ 7.28-7.21 (m, 2H, 3-H, 5-H of -OPh), 6.99-6.88 (m, 1H, 4-H of -OPh), 6.87-6.83 (m, 2H, 2-H, 6-H of -OPh), 6.49 (d, *J* = 2.3 Hz, 2H, 2-H, 6-H), 6.30 (t, *J* = 2.3 Hz, 1H, 4-H), 3.87 (t, *J* = 6.5 Hz, 2H, 6′-H), 3.78 (s, 6H, -OMe), 1.74-1.65 (m, 2H, -CH$_2$- of the side chain), 1.63-1.56 (m, 2H, -CH$_2$- of the side chain), 1.41-1.32 (m, 2H, -CH$_2$- of the side chain), 1.30-1.22 (s, 6H, -C(CH$_3$)$_2$-), 1.18-1.09 (m, 2H, -CH$_2$- of the side chain); ^{13}C NMR (100 MHz CDCl$_3$) δ 160.6 (ArC), 159.2 (ArC), 152.5 (ArC), 129.5 (ArC), 120.6 (ArC), 114.6 (ArC), 104.8 (ArC), 96.8 (ArC), 67.9 (C-6′), 55.3 (-OCH$_3$), 44.5, 38.1, 29.3, 29.1, 26.8, 24.6. Mass spectrum (ESI) *m/z* (relative intensity) 343 (M$^+$+H, 100). LC/MS analysis (Waters MicroMass ZQ system) showed retention time of 5.7 min for the title compound.

5-(7-Bromo-2-methylheptan-2-yl)benzene-1,3-diol (6)(Makriyannis et al., 2007; Makriyannis et al., 2014)
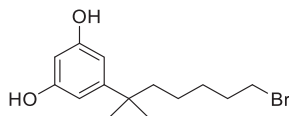
To a stirred solution of **5** (4.60 g, 13.4 mmol) in dry CH$_2$Cl$_2$ (75 mL), at −78°C, under an argon atmosphere, was added 1M boron tribromide solution in CH$_2$Cl$_2$ (59.1 mL, 59.1 mmol) dropwise. Following the addition, the reaction mixture was gradually warmed to room temperature and the stirring was continued at that temperature until completion of the reaction (3 h). The reaction mixture was quenched by the addition of MeOH (75 mL), warmed to room temperature and volatiles were removed in vacuo. The residue was diluted with ethyl acetate and washed sequentially with saturated aqueous NaHCO$_3$ solution, water and brine. The organic layer was dried over MgSO$_4$, filtered and concentrated under reduced pressure. Purification by flash column chromatography on silica gel (10%–35% ethyl acetate in hexanes) afforded 3.98 g of **6** as a white foam in 99% yield. IR (neat) 3323 (br, OH), 2934, 2860, 1599, 1507, 1461, 1438, 1330, 1150, 992, 842, 698 cm^{-1}; ^{1}H NMR (500 MHz, CDCl$_3$) δ 6.37 (s, *J* = 2.0 Hz, 2H, 2-H, 6-H) 6.17 (t, *J* = 2.0 Hz, 1H, 4-H), 4.80 (br s, 2H, -OH), 3.34 (t, *J* = 7.0 Hz, 2H, 6′-H), 1.78 (qt, *J* = 6.9 Hz, 2H, -CH$_2$- of the side chain), 1.58-1.49 (m, 2H, -CH$_2$- of the side chain), 1.38-1.28 (m, 2H, -CH$_2$- of the side chain), 1.23 (s, 6H, -C(CH$_3$)$_2$-), 1.12-1.02 (m, 2H, -CH$_2$- of the side chain); ^{13}C NMR (100 MHz CDCl$_3$) δ 156.2 (ArC), 153.4 (ArC), 106.1 (ArC), 100.3 (ArC), 66.2 (C-6′), 44.2, 37.8, 34.3, 32.7, 28.9, 23.9, 15.0. Mass spectrum (ESI) *m/z* (relative intensity) 301 (M$^+$+H, 100). LC/MS analysis (Waters MicroMass ZQ system) showed retention time of 4.6 min for the title compound.

(1R,4R,5R)-4-[4-(7-Bromo-2-methylheptan-2-yl)-2,6-dihydroxyphenyl]-6,6-dimethylbicyclo[3.1.1]heptan-2-one (7)(Makriyannis et al., 2007)
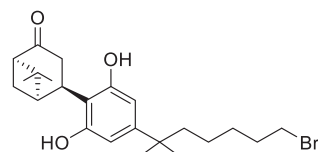
To a degassed solution of **6** (4.71 g, 15.7 mmol) and *p*-toluenesulfonic acid monohydrate (4.79 g, 25.1 mmol) in wet CHCl$_3$ (250 mL) diacetates **18** (6.51 g, ca. 90% pure by ^{1}H NMR, 25.1 mmol(Nikas et al., 2007) was added at 0°C, under an argon atmosphere. The mixture was warmed to room temperature and stirred for 4 d to ensure complete formation of the product. The reaction mixture was diluted with diethyl ether and washed sequentially with water, saturated aqueous NaHCO$_3$ solution, and brine. The organic phase was dried over MgSO$_4$ and the solvent was removed under reduced pressure. The residue was chromatographed on silica gel (15%–50% diethyl ether in hexane) and fractions containing almost pure product (TLC) were combined and evaporated. Further purification by recrystallization from CHCl$_3$ and hexane gave **7** as a white crystalline solid (4.03 g, 59% yield), mp 82-85°C; IR (neat) 3350

(br, OH), 2933, 2868, 1683 (s, > C = O), 1621, 1586, 1419, 1266, 1021, 837, 739, 672 cm^{-1}. ^{1}H NMR (500 MHz, CDCl$_3$) δ 6.28 (s, 2H, Ar-H), 5.34 (br s, 2H, OH), 3.95 (t, J = 8.2 Hz, 1H, 4-H), 3.52 (dd, J = 18.8, 7.7 Hz, 1H, 3α-H), 3.35 (t, J = 6.8 Hz, 2H, 6′-H), 2.67-2.58 (m, 2H, 3β-H, 1-H), 2.55-2.44 (m, 2H, 7α-H, 7β-H), 2.32 (t, J = 5.5 Hz, 1H, 5-H), 1.78 (qt, J = 6.9 Hz, 2H, -CH$_2$- of the side chain), 1.53-1.47 (m, 2H, -CH$_2$- the side chain group), 1.37-1.30 (s and m overlapping, 5H, 6-Me, -CH$_2$- of the side chain, especially 1.36, s, 3H, 6-Me), 1.20 (s, 6H, -C(CH$_3$)$_2$-), 1.13-1.04 (m, 2H, -CH$_2$- of the side chain), 0.99 (s, 3H, 6-Me). ^{13}C NMR (100 MHz CDCl$_3$) δ 217.3 (> C = O), 155.0 (ArC), 149.7 (ArC), 113.8 (ArC), 106.7 (ArC), 58.1, 46.9, 44.3, 42.3, 38.1, 37.4, 34.1, 32.8, 29.7, 29.0, 28.8, 26.3, 24.6, 24.0, 22.3. Mass spectrum (ESI) m/z (relative intensity) 437 (M$^+$+H, 100), 367 (30). LC/MS analysis (Waters MicroMass ZQ system) showed retention time of 5.1 min for the title compound.

(6aR,10aR)-3-(7-Bromo-2-methylheptan-2-yl)-1-hydroxy-6,6-dimethyl-6,6a,7,8,10,10a-hexahydro-9H-benzo[c]chromen-9-one (8)
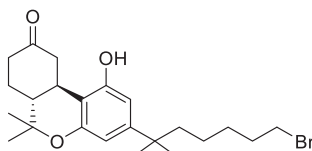

To a stirred solution of **7** (2.04 g, 4.68 mmol) in anhydrous CH$_2$Cl$_2$/CH$_3$NO$_2$ (3:1 mixture, 156 mL) at 0°C, under an argon atmosphere was added trimethylsilyl trifluoromethanesulfonate (4.68 mL, 0.3 M solution in CH$_3$NO$_2$, 1.56 mmol). Stirring was continued for 3 h after the temperature allowed to rise to 25°C. The reaction was quenched with a mixture of saturated aqueous NaHCO$_3$/brine (1:1), and diethyl ether was added. The organic phase was separated, the aqueous phase was extracted with diethyl ether, and the combined organic phase was washed with brine and dried over MgSO$_4$. Solvent evaporation and purification by flash column chromatography on silica gel (15%–30% ethyl acetate-hexane) afforded 1.43 g (75% yield) of the title compound **8** as white foam. IR (neat) 3306 (br, OH), 2935, 2871, 1695 (s, > C = O), 1621, 1576, 1416, 1337, 1139, 1094, 1040, 970, 839 cm^{-1}. ^{1}H NMR (500 MHz, CDCl$_3$) δ 6.37 (d, J = 1.9 Hz, 1H, Ar-H), 6.28 (d, J = 1.9 Hz, 1H, Ar-H), 6.17 (br s, 1H, OH), 4.00 (m as br d, J = 15.1 Hz, 1H, 10eq-H), 3.34 (t, J = 6.9 Hz, 2H, 6′-H), 2.89 (m as td, J = 12.9, 3.5 Hz, 1H, 10a-H), 2.65-2.58 (m, 1H, 8eq-H), 2.50-2.41 (m, 1H, 8ax-H), 2.20-2.12 (m, 2H, 10ax-H, 7eq-H), 1.97 (m as td, J = 11.8, 2.5 Hz, 1H, 6a-H), 1.79 (qt, J = 7.0 Hz, 2H of -CH$_2$- of the side chain), 1.55-1.44 (m and s overlapping, 6H, 7ax-H, -CH$_2$- of the side chain, 6-Me, especially 1.48, s, 3H, 6-Me), 1.33 (qt, J = 7.5 Hz, 2H, -CH$_2$- of the side chain), 1.21 (s, 6H, -C(CH$_3$)$_2$-), 1.13 (s, 3H, 6-Me), 1.12-1.04 (m, 2H, -CH$_2$- of the side chain). ^{13}C NMR (100 MHz CDCl$_3$) δ 214.6 (> C = O), 155.2 (ArC), 154.4 (ArC), 150.5 (ArC), 107.9 (ArC), 107.2 (ArC), 105.6 (ArC), 47.5, 45.1, 44.2, 40.9, 37.5, 34.9, 34.1, 32.8, 28.9, 29.0, 28.9, 28.0, 27.0, 26.9, 19.0. Mass spectrum (ESI) m/z (relative intensity) 437 (M$^+$+H, 100). LC/MS analysis (Waters MicroMass ZQ system) showed retention time of 5.3 min for the title compound.

(6aR,10aR)-3-(7-Bromo-2-methylheptan-2-yl)-1-[(tert-butyldimethylsilyl)oxy]-6,6-dimethyl-6,6a,7,8,10,10a-hexahydro-9H-benzo[c]chromen-9-one (9)
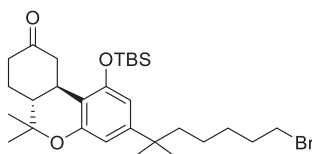

To a solution of **8** (2.52 g, 5.8 mmol) in anhydrous CH$_2$Cl$_2$ (12 mL) under an argon atmosphere were added sequentially, imidazole (395 g, 5.8 mmol), DMAP (73 mg, 0.6 mmol) and TBDMSCI (870 mg, 5.8 mmol). The reaction mixture was stirred room temperature for 12 h. The reaction mixture was diluted with diethyl ether and washed sequentially with 1M aqueous HCl solution, saturated aqueous NaHCO$_3$ solution, water and brine. The organic phase was dried over MgSO$_4$ and the solvent was removed under reduced pressure. Purification by flash column chromatography on silica gel (10%–30% diethyl ether in hexane) afforded 2.65 g (83% yield) of **9** as a colorless oil. IR (neat) 2931, 2859, 1713(s, > C = O), 1613, 1564, 1412, 1332, 1254, 1137, 1096, 1055, 980, 839 cm^{-1}; ^{1}H NMR (500 MHz, CDCl$_3$) δ 6.41 (d, J = 1.9 Hz, 1H, Ar-H), 6.33 (d, J = 1.9 Hz, 1H, Ar-H), 3.77 (ddd, J = 14.9, 3.4, 2.0 Hz, 1H, 10eq-H), 3.33 (t, J = 6.9 Hz, 2H, 6′-H), 2.72 (m as td, J = 12.8, 3.4 Hz, 1H, 10a-H), 2.59-2.52 (m, 1H, 8eq-H), 2.46-2.35 (m, 1H, 8ax-H), 2.2-2.07 (m, 2H, 10ax-H, 7eq-H), 1.95 (m as td, J = 12.5, 3.4 Hz, 1H, 6a-H), 1.78 (qt, J = 6.8 Hz, 2H of -CH$_2$- of the side chain), 1.55-1.44 (m and s overlapping, 6H, 6-Me, 7ax-H, -CH$_2$- of the side chain and especially 1.47, s, 3H, 6-Me), 1.33 (qt, J = 6.8 Hz, 2H, -CH$_2$- of the side chain), 1.21 (s, 3H, -C(CH$_3$)$_2$-), 1.20 (s, 3H, -C(CH$_3$)$_2$-), 1.10-1.03 (m, 2H, -CH$_2$- of the side chain and s, 3H, 6-Me), 1.00 (s, 9H, Si(Me)$_2$CMe$_3$), 0.24 (s, 3H, Si(Me)$_2$CMe$_3$), 0.16 (s, 3H, Si(Me)$_2$CMe$_3$). ^{13}C NMR (100 MHz CDCl$_3$) δ 210.4 (> C = O), 154.8 (ArC-1 or ArC-5), 154.3 (ArC-5 or ArC-1), 149.8 (tertiary aromatic), 112.2 (tertiary aromatic), 109.9 (ArC-2 or ArC-4), 108.5 (ArC-4 or ArC-2), 47.9, 45.7, 44.4, 40.9, 37.5, 35.3, 34.0, 32.9, 29.0, 28.9, 28.8, 28.6, 27.9, 26.2, 25.8, 24.1, 18.8, 18.5, −3.5, −3.9. Mass spectrum (ESI) m/z (relative intensity) 551 (M$^+$+H, 100). LC/MS analysis (Waters MicroMass ZQ system) showed retention time of 6.6 min for the title compound.

{[(6aR,10aR)-3-(7-Bromo-2-methylheptan-2-yl)-9-(methoxymethylene)-6,6-dimethyl-6a,7,8,9,10,10a-hexahydro-6H-benzo[c]chromen-1-yl]oxy}. (tert-butyl)dimethylsilane (10)
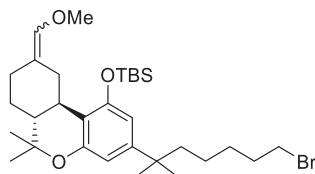
(Methoxymethyl)triphenyl phosphonium chloride (4.31 g, 12.6 mmol) was suspended in 21 mL of dry THF. Potassium bis(trimethyl-silyl)amide (2.42 g, 12.2 mmol) was then added at 0°C, and the reaction mixture was stirred for 20 min at 0°C and for 15 min at room temperature. Intermediate **9** (1.16 g, 2.1 mmol) was dissolved in 5 mL of dry THF and added dropwise to the solution of the red ylide at 0°C. The reaction mixture was stirred at 0°C to room temperature for 1.5 h, and then quenched with saturated aqueous NH$_4$Cl solution at 0°C and diluted with diethyl ether. The organic layer was separated and the aqueous layer was extracted with diethyl ether. The combined organic layer was washed with brine, dried (MgSO$_4$), and concentrated in vacuo. The residue was chromatographed on silica gel (0%–10% diehtyl ether in hexane) to give a mixture (**10**) of two geometrical isomers **10a** and **10b** (1.71 g, 71% yield) as a colorless oil in the ratio of 2:1 respectively as determined by ^{1}H NMR analysis. IR (neat) 2931, 2859, 1684, 1611, 1561, 1411, 1251, 1120, 1097, 1053, 980, 836, 779, 742, 695 cm^{-1}. ^{1}H NMR (400 MHz, CDCl$_3$) 6.37 (d, J = 1.9 Hz, 1H, Ar-H, **10a**), 6.36 (d, J = 1.9 Hz, 1H, Ar-H, **10b**), 6.32 (d, J = 1.9 Hz, 1H, Ar-H, **10b**), 6.31 (d, J = 1.9 Hz, 1H, Ar-H, **10a**), 5.86 (s, 1H, = C*H*OMe, **10a**), 5.81 (s, 1H, = C*H*OMe, **10b**), 4.22-4.15 (m as dd, J = 13.6, 3.4 Hz, 1H, C-ring, **10b**), 3.55 (s, 3H, OMe, **10a**), 3.52 (s, 3H, OMe, **10b**), 3.46-3.42 (m as dd, J = 13.6, 3.4 Hz, 1H, C-ring, **10a**), 3.32 (t, J = 6.9 Hz, 2H, 6′-H for **10a** and 2H, 6′-H for **10b**), 2.96-2.88 (m as br d, J = 13.6 Hz, 1H, C-ring, **10a**), 2.35-2.26 (m, 1H, C-ring of **10a** and 1H, C-ring of **10b**), 2.22-2.15 (m, 1H, C-ring, **10b**), 2.09-1.99 (m, 1H, C-ring, **10b**), 1.92-1.84 (m, 1H, C-ring of **10a** and 1H, C-ring of **10b**), 1.83-1.72 (m, 1H, C-ring, **10a**), 1.69-1.55 (m, 2H, -CH$_2$- of the side chain of **10a**, 2H, -CH$_2$- of the side chain of **10b**, 2H, C-ring of **10a**, and 2H, C-ring of **10b**), 1.55-1.46 (m, 2H, -CH$_2$- of the side chain of **10a**, 2H, -CH$_2$- of the side chain of **10b**), 1.39 (s, 3H, 6-Me, **10a**), 1.38 (s, 3H, 6-Me, **10b**), 1.32 (qt, J = 7.2 Hz, 2H, -CH$_2$- of the side chain of **10a**, 2H, -CH$_2$- of the side chain of **10b**), 1.20 (s, 6H, -C(CH$_3$)$_2$- of **10a**), 1.19 (s, 6H, -C(CH$_3$)$_2$- of **10b**), 1.12-0.97 (m, s, s, s, and s, overlapping, 1H, C-ring of **10a**, 1H, C-ring of **10b**, 2H, -CH$_2$- of the side chain of **10a**, 2H, -CH$_2$- of the side chain of **10b**, 3H, 6-Me of **10a**, 3H, 6-Me of **10b**, 9H, -Si(Me)$_2$C*Me*$_3$, of **10a**, 9H, -Si(Me)$_2$C*Me*$_3$, of **10b**, especially 1.03, s, -Si(Me)$_2$C*Me*$_3$, of **10a** and 1.00, s, -Si(Me)$_2$C*Me*$_3$, of **10b**), 0.24 (s, 3H, -Si(*Me*)$_2$CMe$_3$, **10a**), 0.23 (s, 3H, -Si(*Me*)$_2$CMe$_3$, **10b**), 0.19 (s, 3H, -Si(*Me*)$_2$CMe$_3$, **10b**), 0.15 (s, 3H, -Si(*Me*)$_2$CMe$_3$, **10a**). Mass spectrum (ESI) *m/z* (relative intensity) 579 (M$^+$+H, 100). LC/MS analysis (Waters MicroMass ZQ system) showed retention time of 7.2 min for the title compound.

(6aR,10aR)-3-(7-Bromo-2-methylheptan-2-yl)-1-[(tert-butyldimethylsilyl)oxy]-6,6-dimethyl-6a,7,8,9,10,10a-hexahydro-6H-benzo[c]chromene-9-carbaldehyde (11)
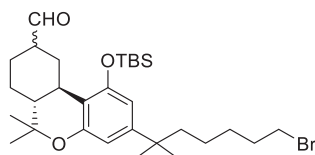
To a stirred solution of **10** (2.50 g, 4.3 mmol) in CH$_2$Cl$_2$ (144 mL) under an argon atmosphere, was added wet trichloroacetic acid (3.51 g, 21.6 mmol). The reaction mixture was stirred at room temperature for 50 min and then quenched with saturated aqueous NaHCO$_3$ solution and diluted with diethyl ether. The organic layer was separated and the aqueous layer was extracted with diethyl ether. The combined organic phase was washed with water and brine, dried (MgSO$_4$) and evaporated under reduced pressure. The residue consisted of a mixture of epimeric aldehydes **12** and **11a** (2.26 g, 93% yield) in the ratio of 2:1 respectively as determined by ^{1}H NMR analysis, and it was used into the next step as such. ^{1}H NMR (500 MHz, CDCl$_3$) δ 9.89 (d, J = 1.5 Hz, 1H, 9α-CHO, **11a**), 9.63 (d, J = 1.5 Hz, 1H, 9β-CHO, **12**), 6.38 (d, J = 1.9 Hz, 1H, Ar-H, **12**), 6.36 (d, J = 1.9 Hz, 1H, Ar-H, **11a**), 6.33 (d, J = 1.9 Hz, 1H, Ar-H, **11a**), 6.32 (d, J = 1.9 Hz, 1H, Ar-H, **12**), 3.69-3.62 (m as br d, J = 14.0 Hz, 1H, C-ring, **11a**), 3.52-3.44 (m, 1H, C-ring, **12**), 3.33 (t, J = 6.5 Hz, 2H, -CH$_2$Br for **12** and 2H, -CH$_2$Br for **11a**), 2.65-2.60 (m, 1H, C-ring, **11a**), 2.45-2.33 (m, 2H, C-ring, **12** and 2H, C-ring, **11a**), 2.31-2.24 (m, 1H, C-ring, **11a**), 2.14-2.07 (m, 1H, C- ring, **12**), 2.03-1.96 (m, 1H, C-ring, **12**), 1.80-1.71 (m, 2H, -CH$_2$- of the side chain 1H of **12**, 2H, -CH$_2$- of the side chain of **11a**),1.65-1.60 (m, 1H, C-ring, **12**, 1H, C-ring, **11a**), 1.58-1.42 (m, 2H, -CH$_2$- of the side chain of **12**, 2H, -CH$_2$- of the side chain of **11a**, 1H, C-ring of **12**, 1H, C-ring of **11a**), 1.39 (s, 3H, 6-Me of **12**), 1.35 (s, 3H, 6-Me of **11a**), 1.33 (qt, J = 7.5 Hz, 2H, -CH$_2$- of the side chain of **12** and 2H, -CH$_2$- of the side chain of **11a**), 1.25-1.11 (m, 2H, C-ring of **12**, 1H, C-ring of **11a**, 6H, -C(CH$_3$)$_2$- of **11a**, 6H, -C(CH$_3$)$_2$- of **12**), 1.09-1.03 (m and s, overlapping, 2H, -CH$_2$- of the side chain of **12**, 2H, -CH$_2$- of the side chain

of **11a**, 1.07, s, 3H, 6-Me, **12**), 1.02-1.00 (s and s overlapping, 3H, 6-Me of **11a** and 9H, -Si(Me)$_2$C*Me*$_3$ of **12**), 0.97 (s, 9H, -Si(Me)$_2$-C*Me*$_3$, **11a**), 0.28 (s, 3H, -Si*(Me)*$_2$CMe$_3$, **11a**), 0.26 (s, 3H, Si*(Me)*$_2$CMe$_3$, **12**), 0.25 (s, 3H, Si*(Me)*$_2$CMe$_3$, **11a**), 0.15 (s, 3H, Si*(Me)*$_2$CMe$_3$, **12**).

(6aR,9R,10aR)-3-(7-Bromo-2-methylheptan-2-yl)-1-[(tert-butyldimethylsilyl)oxy]-6,6-dimethyl-6a,7,8,9,10,10a-hexahydro-6H-benzo[c]chromene-9-carbaldehyde (12)
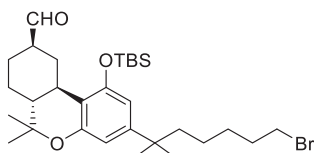

To a mixture of **11a** and **12** (2.20 g, 3.9 mmol) in ethanol (77 mL) under an argon atmosphere, was added potassium carbonate powder (2.68 g, 19.4 mmol) and the mixture was stirred at room temperature for 3 h. The reaction mixture was quenched by the dropewise addition of 1M aqueous acetic acid solution (until pH of 5). The volatiles were evaporated under reduced pressure. The water layer was extracted with diethyl ether. The organic layer was washed with brine, dried (MgSO$_4$), and concentrated under reduced presure. Purification by flash column chromatography on silica gel (5%–25% diethyl ether in hexane) gave **12** (1.78 g, 81% yield) as a colorless oil. IR (neat) 2934, 2860, 2713 (w, CHO), 1728 (s, > C = O), 1613, 1560, 1413, 1331, 1253, 1066, 982, 838, 780 cm^{-1}. ^{1}H NMR (500 MHz, CDCl$_3$) δ 9.63 (d, J = 1.5 Hz, 1H, 9β-CHO), 6.38 (d, J = 1.9 Hz, 1H, Ar-H), 6.32 (d, J = 1.9 Hz, 1H, Ar-H), 3.52-3.44 (m, 1H, C-ring), 3.33 (t, J = 6.9 Hz, 2H, 6'-H), 2.45-2.36 (m as td, J = 11.0, 2.6 Hz, 2H, C-ring), 2.14-2.06 (m, 1H, C-ring), 2.03-1.95 (m, 1H, C-ring), 1.77 (qt, J = 7.2 Hz, 2H, -CH$_2$- of the side chain), 1.64-1.60 (m, 1H, C-ring), 1.54-1.46 (m, 3H, -CH$_2$- of the side chain, C-ring), 1.39 (s, 3H, 6-Me), 1.32 (qt, J = 7.5 Hz, 2H, -CH$_2$- of the side chain), 1.26-1.18 (m, 2H, C-ring, and 6H, -C(CH$_3$)$_2$-), 1.09-0.99 (m, s, and s, overlapping, 14H as follows: 2H, -CH$_2$- of the side chain, 1.08, s, 3H, 6-Me, 1.01, s, 9H, -Si(Me)$_2$C*Me*$_3$), 0.26 (s, 3H, Si*(Me)*$_2$CMe$_3$), 0.15 (s, 3H, Si*(Me)*$_2$CMe$_3$). ^{13}C NMR (100 MHz CDCl$_3$) δ 203.6 (-CHO), 154.6 (ArC-1 or ArC-5), 154.3 (ArC-5 or ArC-1), 149.3 (tertiary aromatic), 112.6 (tertiary aromatic), 109.6 (ArC-2 or ArC-4), 108.5 (ArC-4 or ArC-2), 50.6, 49.1, 44.3, 37.4, 37.3, 35.5, 33.9, 32.8, 30.2, 28.9, 28.8, 28.7, 27.6, 26.9, 26.0, 25.9, 23.9, 18.8, 18.2, −3.6, −4.2. Mass spectrum (ESI) m/z (relative intensity) 565 (M$^+$+H, 100). LC/MS analysis (Waters MicroMass ZQ system) showed retention time of 6.8 min for the title compound.

{(6aR,9R,10aR)-3-(7-Bromo-2-methylheptan-2-yl)-1-[(tert-butyldimethylsilyl)oxy]-6,6-dimethyl-6a,7,8,9,10,10a-hexahydro-6H-benzo[c]chromen-9-yl}methanol (13)
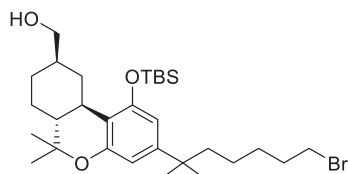
Sodium borohydride (394 mg, 10.5 mmol) was added to a stirred solution of aldehyde **12** (740 mg, 1.31 mmol) in ethanol (32 mL) at 0°C under argon. After 30 min, the reaction was quenched with the addition of saturated aqueous NH$_4$Cl solution and volatiles were removed in vacuo. The residue was dissolved in ethyl acetate and water was added. The organic layer was separated and the aqueous layer was extracted with ethyl acetate. The combined organic phase was washed with water and brine, dried (MgSO$_4$), and evaporated. Purification by flash column chromatography on silica gel (15%–50% diethyl ether in hexane) gave **13** (712 mg, 96% yield) as a colorless viscous oil. IR (neat) 3360 (br, OH), 2935, 2869, 1743, 1621, 1560, 1415, 1364, 1217, 1139, 1038, 971, 837, 748 cm^{-1}; ^{1}H NMR (400 MHz, CDCl$_3$) δ 6.37 (d, J = 1.9 Hz, 1H, Ar-H), 6.30 (d, J = 1.9 Hz, 1H, Ar-H), 3.54 (dd, J = 10.6, 5.6 Hz, half of an AB system, 1H, -CH$_2$OH), 3.50-3.43 (m as dd, J = 10.6, 6.5 Hz, half of an AB system, 1H, -CH$_2$OH), 3.32 (t, J = 6.9 Hz, 2H, 6'-H), 3.19-3.13 (m as br d, J = 12.8 Hz, 1H, C-ring), 2.40-2.32 (m as td, J = 11.0, 2.6 Hz, 1H, C-ring), 2.04-1.88 (m, 2H, C-ring), 1.81-1.59 (m, 3H as follows 1H of C-ring, 2H, -CH$_2$- of the side chain), 1.54-1.43 (m, 3H, -CH$_2$- of the side chain, C-ring), 1.38 (s, 3H, 6-Me), 1.35-1.27 (m, 3H, -CH$_2$- of the side chain, C-ring) 1.20 (s, 3H, -C(CH$_3$)$_2$-), 1.19 (s, 3H, -C(CH$_3$)$_2$-), 1.17-1.10 (m, 3H, -CH$_2$- of the side chain, C-ring), 1.06 (s, 3H, 6-Me), 1.00 (s, 9H, Si(Me)$_2$C*Me*$_3$), 0.77 (q, J = 11.9 Hz, 1H, C-ring), 0.23 (s, 3H, Si*(Me)*$_2$CMe$_3$), 0.13 (s, 3H, Si*(Me)*$_2$CMe$_3$). ^{13}C NMR (100 MHz CDCl$_3$) δ 154.7 (ArC-1 or ArC-5), 154.4 (ArC-5 or ArC-1), 149.0 (tertiary aromatic), 113.8 (tertiary aromatic), 109.8 (ArC-2 or ArC-4), 108.6 (ArC-4 or ArC-2), 68.6 (-CH$_2$OH), 49.8, 44.5, 41.9, 40.7, 37.4, 35.7, 33.4, 32.7, 29.9, 29.5, 29.0, 28.9, 27.8, 27.7, 26.1, 24.1, 19.0, 18.4, −3.4, −4.1. Mass spectrum (ESI) m/z (relative intensity) 567 (M$^+$+H, 100). LC/MS analysis (Waters MicroMass ZQ system) showed retention time of 6.5 min for the title compound.

7-[(6aR,9R,10aR)-1-Hydroxy-9-(hydroxymethyl)-6,6-dimethyl-6a,7,8,9,10,10a-hexahydro-6H-benzo[c]chromen-3-yl]-7-methyloctanenitrile (AM12033)
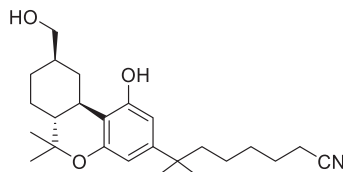
To a solution of **13** (120 mg, 0.21 mmol) in anhydrous DMSO (4.2 mL), under an argon atmosphere, was added NaCN (103.1 mg, 2.1 mmol). The reaction mixture was stirred for 9 h at room temperature, and then quenched with the addition of ice. Extractive isolation with diethyl ether, and purification by flash column chromatography on silica gel (20%–50% ethyl acetate in hexane) gave **AM12033** (66 mg, 79% yield) as a white solid. Melting point = 73°C. IR (neat) 3382 (br, OH), 2932, 2864, 2252 (w, CN), 1621, 1574, 1461, 1414, 1333, 1271, 1139, 1038, 971, 839, 736 cm^{-1}; ^{1}H NMR (400 MHz, CDCl$_3$) δ 6.33 (d, *J* = 1.9 Hz, 1H, Ar-H), 6.20 (d, *J* = 1.9 Hz, 1H, Ar-H), 5.25 (br s, 1H, OH), 3.53 (d, *J* = 6.3 Hz, 2H, -C*H*$_2$OH), 3.24-3.17 (m as br d, *J* = 12.8 Hz, 1H, C-ring), 2.48 (td, *J* = 11.1, 2.8 Hz, 1H, C-ring), 2.26 (t, *J* = 7.1 Hz, 2H, 6'-H), 2.00-1.89 (m, 2H, C-ring), 1.84-1.72 (m, 1H, C-ring), 1.61-1.55 (m, 3H, -CH$_2$- of the side chain, C-ring), 1.54-1.48 (m, 3H, -CH$_2$- of the side chain, C-ring), 1.40-1.30 (s and qt overlapping, 2H, -CH$_2$- of the side chain, especially 1.38, s, 3H, 6Me), 1.20 (s, 6H, -C(CH$_3$)$_2$-), 1.18-1.03 (s and m overlapping, 2H, -CH$_2$- of the side chain, 1H, C-ring, especially, 1.08, s, 3H, 6-Me), 0.83 (q, *J* = 11.9 Hz, 1H, C-ring); ^{13}C NMR (100 MHz CDCl$_3$) δ 154.9 (ArC-1 or ArC-5), 154.8 (ArC-5 or ArC-1), 149.4 (tertiary aromatic), 120.0 (-CN), 109.9 (tertiary aromatic), 108.0 (ArC-2 or ArC-4), 105.5 (ArC-4 or ArC-2), 68.7 (-CH$_2$OH), 49.5, 44.1, 40.6, 37.4, 35.1, 33.3, 29.9, 29.3, 28.9, 28.8, 27.9, 27.6, 25.3, 23.9, 19.2, 17.2 (-CH$_2$CN). Exact mass (ESI) calculated for C$_{25}$H$_{38}$NO$_3$ (M$^+$ + H), 400.2852; found 400.2853. LC/MS analysis (Waters MicroMass ZQ system) showed retention time of 5.2 min for the title compound.

Protein Engineering and Expression of CB2 for Crystallography Study

CB2-T4L construction and expression for crystallization were performed using the similar procedure as described before(Li et al., 2019). In brief, the construct has truncations of residues 1-20, 223-234 and 326-360; the T4L fusion protein was fused to the truncated third intracellular loop of the human CB2 gene. Six mutations (Gly78$^{2.48}$Leu, Thr127$^{3.46}$Ala, Thr153$^{4.45}$Leu, Gly210$^{5.59}$Ala, Arg242$^{6.32}$Glu and Gly304$^{8.48}$Glu) were introduced into the CB2-T4L gene for further modification. The optimized construct was cloned into a modified pFastBac1 vector with the haemagglutinin (HA) signal sequence at the N terminus and a 10 × His-tag followed by a Flag-tag at the C terminus. The modified CB2–T4L protein was expressed in Spodoptera frugiperda (*Sf*9) insect cells using the Bac-to-Bac Baculovirus Expression System (Invitrogen). *Sf*9 cells were infected at a cell density of 2-2.5 × 10^6 cells per ml with high-titer viral stock MOI (multiplicity of infection) of 5.0. Cells were harvested by centrifugation for 48 h post-infection and stored at −80°C for future use.

CB2-AM12033 Complex Purification for Co-crystallization

Frozen cell pellets were thawed and lysed by repeated washing and centrifugation in the hypotonic buffer of 10 mM HEPES (pH 7.5), 10 mM MgCl$_2$, 20 mM KCl, and the high osmotic buffer of 10 mM HEPES (pH 7.5), 1.0 M NaCl, 10 mM MgCl$_2$, 20 mM KCl, with EDTA-free complete protease inhibitor cocktail tablets (Roche). Purified membranes were thawed at room temperature and incubated with 20 μM AM12033 and inhibitor cocktail at 4°C for 3 h. The membranes were further incubated with 1.0 mg/mL iodoacetamide (Sigma) for 1 h and were solubilized in the buffer containing 50 mM HEPES (pH 7.5), 500 mM NaCl, 0.75% (w/v) lauryl maltose neopentyl glycol (LMNG, Anatrace) and 0.15% (w/v) cholesterol hemisucinate (CHS, Sigma-Aldrich) at 4°C for 2.5-3 h. The supernatant was isolated by ultracentrifugation, and then incubated with TALON IMAC resin (Clontech) and 20 mM imidazole, at 4°C overnight. The resin was washed with 15 column volumes (CV) of washing buffer I containing 25 mM HEPES (pH 7.5), 500 mM NaCl, 10% (v/v) glycerol, 0.1% (w/v) LMNG, 0.02% (w/v) CHS, 30 mM imidazole and 20 μM AM12033, and 10 CV of washing buffer II containing 25 mM HEPES (pH 7.5), 500 mM NaCl, 10% (v/v) glycerol, 0.03% (w/v) LMNG, 0.006% (w/v) CHS, 50mM imidazole and 20 μM AM12033. The protein was eluted using 3 CV of elution buffer containing 25 mM HEPES (pH7.5), 500 mM NaCl, 10% (v/v) glycerol, 0.01% (w/v) LMNG, 0.002% (w/v) CHS, 250 mM imidazole and 25 μM AM12033. The purified receptor was then concentrated to 20 mg/mL for crystallization trials.

Crystallization of CB2-AM12033 in Lipidic Cubic Phase

Crystallization was performed using the lipidic cubic phase (LCP) method as described before(Caffrey and Cherezov, 2009). The concentrated CB2 protein in complex with AM12033 was reconstituted into LCP by mixing with molten lipid (90% (w/v) monoolein and 10% (w/v) cholesterol at volume ratio of 2:3 using a syringe mixer. LCP crystallization trials were performed using an NT8-LCP crystallization robot (Formulatrix). 96-well sandwich plates were incubated and imaged at 20°C using an automated incubator/imager (RockImager, Formulatrix). Crystals grew in the condition of 100 mM HEPES pH 7.0, 25% PEG 400, 220 mM Sodium sulfate

decahydrate, and reached a full size of 40 mm × 20 mm after 2 weeks. The crystals were harvested from the LCP matrix using micromounts (MiTeGen) and immediately flash frozen in liquid nitrogen.

Data Collection and Structure Determination of CB2-AM12033

X-ray diffraction data were collected at the Spring-8 beamline 41XU, using a Pilatus3 6M detector (X-ray wavelength 1.0000 Å). A rastering and data-collection strategy was followed as previously described (Cherezov et al., 2009). Diffraction images were indexed, integrated, and scaled using XDS (Kabsch, 2010) and merged using XPREP. Initial phases were obtained by molecular replacement (MR) with Phaser (McCoy et al., 2007) using the antagonist AM10257 bound CB2 structure (PDB: 5ZTY) as search model. The structure determination was completed by manually modeling the CB2 and T4L in the program COOT (Emsley et al., 2010) using both |$2F_o|-|F_c|$ and |$F_o|-|F_c|$ maps and refined with Phenix (Adams et al., 2010) and Buster (Smart et al., 2012).

Constructs and Expression of CB2 and G_i Heterotrimer

The N-BRIL fused wild type human CB2 construct was cloned into a modified pFastBac1 vector with the HA signal sequence at the N terminus followed by a 10 × His-tag and a Flag-tag. Human $G_{\alpha i1}$ and $G_{\beta1\gamma2}$ subunits were cloned into pFastbac1 and pFastDual vector individually. The CB2 and G_i heterotrimer were co-expressed in $Sf9$ insect cells using the Bac-to-Bac Baculovirus Expression System (Invitrogen). $Sf9$ cells were infected at a cell density of 2-2.5 × 10^6 cells per ml with three separate virus preparations for CB2, $G_{\alpha i1}$ and $G_{\beta1\gamma2}$ at a ratio of 1:2:2. The infected cells were cultured at 27°C for 48 h before collection by centrifugation and the cell pellets were stored at −80°C for future use.

Constructs, Expression, and Purification of scFv16

ScFv16 was cloned into a modified pFastBac1 vector containing a GP67 secretion signal before the amino terminus of the scFv16 and 10 × His tag at C terminus. ScFv16 expressed in secreted form from Trichuplusia ni Hi5 insect cells using the Bac-to-Bac Baculovirus Expression System, and purified by Ni-NTA chromatography. Supernatant was pH balanced by addition of 1M Tris pH 8.0, and then was loaded onto Ni-NTA resin. The column was washed with 6 CV wash buffer I 20 mM HEPES pH 7.5, 100 mM NaCl, and 10 mM imidazole followed by 4 CV wash II 20 mM HEPES pH 7.5, 100 mM NaCl, and 30 mM imidazole. The protein was eluted with the same buffer supplemented with 250 mM imidazole, the C-terminal 10 × His tag was cleaved by incubation with human rhinovirus 3C protease, and the protein was dialyzed into a buffer consisting of 20 mM HEPES pH 7.5 and 100 mM NaCl. Cleaved scFv16 was further purified by reloading over Ni-NTA resin. The flowthrough was collected and purified over gel filtration chromatography using a Hiload Superdex 7510/300 column. Monomeric fractions were pooled, concentrated, and flash frozen in liquid nitrogen, then stored at −80°C for further use.

CB2-G_i-scFv16 Complex Formation and Purification

The cell pellets corresponding to 1L CB2-Gi co-expression culture were thawed and lysed in the hypotonic buffer of 10mM HEPES, pH7.5, 10 mM $MgCl_2$, 20 mM KCl with EDTA-free complete protease inhibitor cocktail tablets (Roche). The CB2-Gi complex was formed in membranes by addition of 20 μM AM12033 and 2 units of apyrase (NEB) in the presence 500 ug scFv16. The lysate was incubated for overnight at 4°C and discard the supernatant by centrifugation at 40,000 × rpm for 30min. The complex from membranes was solubilized in the buffer containing 50 mM HEPES (pH 7.5), 100 mM NaCl, 0.75% (w/v) lauryl maltose neopentyl glycol (LMNG, Anatrace), 0.15% (w/v) cholesterol hemisuccinate (CHS, Sigma-Aldrich), 20 μM AM12033 and 2 units of apyrase (NEB) at 4°C for 2 h. The supernatant was isolated by ultracentrifugation, and then incubated with TALON IMAC resin (Clontech) and 20 mM imidazole over 6 h at 4°C. The resin was washed with 15 CV (column volumes) of washing buffer I containing 25 mM HEPES (pH 7.5), 100 mM NaCl, 10% (v/v) glycerol, 0.1% (w/v) LMNG, 0.02% (w/v) CHS, 30 mM imidazole and 20 μM AM12033, and 15 column volumes of washing buffer II containing 25 mM HEPES (pH 7.5), 100 mM NaCl, 10% (v/v) glycerol, 0.03% (w/v) LMNG, 0.006% (w/v) CHS, 50mM imidazole and 20 μM AM12033. The protein was eluted using 3 column volumes of elution buffer containing 25mM HEPES (pH 7.5), 100 mM NaCl, 10% (v/v) glycerol, 0.01% (w/v) LMNG, 0.002% (w/v) CHS, 250 mM imidazole and 25 μM AM12033. The purified CB2-Gi complex was concentrated, then injected onto a Superdex200 10/300 GL column (GE Healthcare) equilibrated in the buffer containing 20 mM HEPES, pH 7.5, 100 mM NaCl, 0.00075% (w/v) LMNG, 0.00025% GDN, 0.0001% (w/v) CHS, 100 μM TCEP. The complex peak fractions were collected and concentrated individually to 0.8-1.0 mg/mL for electron microscopy experiments.

CB1-G_i-scFv16 Complex Expression, Formation, and Purification

Wild type human CB1 was subcloned into a modified mammalian expression pTT5 vector, which contains a haemagglutinin (HA) signal sequence, a FLAG tag and 10 × His tag, followed by a tobacco etch virus (TEV) protease cleavage site. In order to improve the protein expression, the construct was further modified by the truncations of the CB1 residues 1-70, and 426-472, and the BRIL (PDB: 1M6T, MW 10.9kDa) fusion protein was fused to the N terminus. Glu273[5.37]Lys, Thr283[5.47]Val and Arg340[6.32]Glu, which do not affect the G protein-coupling were introduced (Hua et al., 2017). The protein expression and membrane preparation were performed using the same procedure as described before (Hua et al., 2017). Purified membranes were thawed at room temperature and then incubated with 25 μM AM841 in the presence of 1.0 mg/mL iodoacetamide (Sigma) and EDTA-free protease inhibitor cocktail (Roche) at 4°C for 2 h. The membranes were then solubilized with 50 mM HEPES (pH 7.5), 100 mM NaCl, 1% (w/v) LMNG, 0.2% (w/v) CHS at

4°C for 2.5-3 h. The supernatants were isolated by high-speed centrifugation, and then incubated with TALON IMAC resin and 20 mM imidazole, at 4°C overnight. The resin was washed with 15 column volumes of washing buffer I containing 25 mM HEPES (pH 7.5), 100 mM NaCl, 10% (v/v) glycerol, 0.1% (w/v) LMNG, 0.02% (w/v) CHS, 30 mM imidazole and 20 uM AM841, and 5 column volumes of washing buffer II containing 25 mM HEPES (pH 7.5), 100 mM NaCl, 10% (v/v) glycerol, 0.03% (w/v) LMNG, 0.006% (w/v) CHS, 50mM imidazole and 20 uM AM841. The proteins were eluted by 2.5 column volumes of eluting buffer containing 25 mM HEPES (pH 7.5), 100 mM NaCl, 10% (v/v) glycerol, 0.01% (w/v) LMNG, 0.001% (w/v) CHS, 250 mM imidazole and 20 uM AM841. PD MiniTrap G-25 column was used to remove imidazole and the protein was used for the complex formation.

Heterotrimeric G-proteins were expressed and purified as follows: Human $G_{\alpha i1}$ and $G_{\beta 1 \gamma 2}$ subunits were cloned into pFastbac1 and pFastDual vector individually. *Sf9* insect cells were coinfected with viruses encoding $G_{\alpha i1}$ and $G_{\beta 1 \gamma 2}$ subunits. In order to facilitate the purification, His-tag with TEV cleavable site is attached at the amino terminus of the G_γ subunit. Cells were harvested 48 h post infection, lysed in hypotonic buffer containing 50 mM HEPES (pH 7.5), 100 mM NaCl, protease inhibitor, 5 mM imidazole, 5 mM $MgCl_2$, 1mM DTT. The supernatant was purified by nickel affinity chromatography, followed by size-exclusion chromatography using a Superdex 75 column. Monomeric fractions were pooled, concentrated for complex formation.

CB1-Gi-scFv16 complex formation: purified receptors and excess molar ratio of G-protein were mixed together. The coupling reaction was allowed to proceed at 24°C for 1 h and was followed by addition of apyrase to catalyze hydrolysis of unbound GDP. And then the incubated at 25°C for another 2 h. Finally, a 1.2 molar excess of scFv16 was added to the complex and incubated at 4°C overnight. The CB1-G_i-scFv16 complex was purified by size exclusion chromatography on a superdex 200 10/300 GL column in 20 mM HEPES, pH 7.5, 100 mM NaCl, 0.00075% (w/v) LMNG, 0.00025% GDN, 0.0001% (w/v) CHS, 100 μM TCEP and 5 μM AM841. Peak fractions were concentrated to 1 mg/mL for electron microscopy studies.

Cryo-EM Sample Preparation and Image Acquisition

Three microliters of purified CB1-G_i-scFv16 or CB2-G_i-scFv16 complexes was applied to a glow-discharged holey carbon grid (CryoMatrix Amorphous alloy film R1.2/1.3, 300 mesh), and subsequently vitrified using a Vitrobot Mark IV (Thermo Fisher Scientific). The chamber of Vitrobot was set to 100% humidity at 4°C. The sample was blotted for 2.5 s with blot force 2. Cryo-EM images were collected on a Titan Krios microscope operated at 300 kV equipped with a Gatan Quantum energy filter, with a slit width of 20 eV, a Gatan K2 summit direct electron camera (Gatan). Movies were taken in EFTEM nanoprobe mode, with 50 μm C2 aperture, at a calibrated magnification of 130,000 corresponding to a magnified pixel size of 1.04 E. Each movie comprises 45 frames with a total dose of 60 electrons per E^2, exposure time was 8.1 s with the dose rate of 8e$^-$/ Å^2/s. Data acquisition was done using SerialEM software (Mastronarde, 2005) with a defocus range of −0.8 to −2.0 μm.

Image Processing and 3D Reconstruction

For CB1-G_i-scFv16 complex, a total of 5577 movies were collected and subjected for motion correction using MotionCor2 (Zheng et al., 2017). Contrast transfer function (CTF) parameters for each non-dose weighted micrography were estimated by Gctf (Zhang, 2016). Particles selection, 2D and 3D classifications were performed on a binned dataset with a pixel size of 2.08 Å using RELION 2.1.0 (Scheres, 2012). To generate CB1-G_i-scFv16 complex template for automatic picking, around 2,186,340 particles were automatically picked with manual guidence and classified by 2D classification in RELION. After auto-picking in RELION, the low-quality images and false-positive particles were removed manually. About 1,385,539 particles were extracted for subsequent processing. We used the cryo-EM structure of CB1-FUB-G_i complex (Electron Microscopy Data Bank code EMD-0339), low-pass-filtered to 60 Å, as the initial model for 3D classification in RELION. The model of the best class after 3D classification was used as the initial model for the final 3D classification and 3D auto-refinement. Further Baycsian polishing of these particles was performed in RELION3.0, followed by another round of auto-refinement, which generated a final 3.0 Å map determined by gold standard Fourier shell correlation using the 0.143 criterion. Local resolution estimation was performed with the Bsoft package (Heymann, 2001) using the two unfiltered half maps.

For CB2-G_i-scFv16 complex, a total of 3894 images were collected. The dataset was subjected to motion correction, CTF estimation, autopicking, 2D classification and 3D classification in RELION 2.1.0. About 1,248,405 particles were extracted for further 3D processing. We used our cryo-EM structure of CB1-AM841-G_i complex, low-pass-filtered to 60 Å, as the initial model for 3D classification in RELION. After auto-refinement and further Baycsian polishing applied to these particles in RELION3.0 improved the density map with nominal resolution of 2.9 Å. Local resolution estimation was also performed with the Bsoft package.

Model Building and Refinement

For CB1-G_i-scFv16 complex, the cryo-EM structure of CB1-FUB-G_i complex (PDB code 6N4B) was used as the starting model for model building and refinement against the electron density map. For CB2-G_i-scFv16 complex, the CB2-AM12033 crystal structure and G_i protein in CB1 were used as the starting model. The model was docked into the EM density map using Chimera (Pettersen et al., 2004), followed by iterative manual adjustment and rebuilding in COOT (Emsley et al., 2010) and phenix.real_space_refine in Phenix (Adams et al., 2010). The model statistics were validates using MolProbity (Chen et al., 2010a). Structural figures were prepared in Chimera and PyMOL (https://pymol.org/2/). The final refinement statistics are provided in Table S1. The extent of any model overfitting during refinement was measured by refining the final model against one of the half-maps and by comparing the resulting map versus model FSC curves with the two half-maps and full model.

Molecular Docking

The Schrodinger Suite 2018-4 (Schrödinger) was used to predict the ligand-binding poses for CB1 or CB2. The structures of the two receptors were processed by using the 'Protein Preparation Wizard' (Sastry et al., 2013) and converting of ligands from 2D to 3D structures was carried out using 'LigPrep' (Schrödinger). The 'Glide' SP was used in molecular docking (Friesner et al., 2004; Friesner et al., 2006).

Molecular Dynamics Simulation of CB1/CB2 in Complex with Agonists

The CB1 and CB2 structures were isolated from their cryo-EM complex structures and Prime (Schrödinger) was used to add missing side chains, hydrogens and cap the termini of the receptors. The residues $D163^{2.50}$, $D213^{3.49}$ in CB1, $D80^{2.50}$, $D130^{3.49}$ in CB2 were manually protonated to simulate the protonation upon GPCR activation (Ranganathan et al., 2014). Then the processed CB1 or CB2 in complex with agonists (AM841, HU-308 or L-759,656) was embedded in a bilayer composed of 140 1-palmitoyl-2-oleoyl-sn-glyc-ero-3-phosphocholine (POPC) lipids using the CHARMM-GUI Membrane Builder (23, 24). The orientation of CB1 or CB2 in the membrane is referenced to the CB1 structure (PDB: 5TGZ) in the Orientations of Proteins in Membranes (OPM) database (25). Each receptor-agonist-membrane system was solvated in a periodic 0.15 M NaCl TIP3P water box with a minimum water height of 20.0 Å on top and bottom of the system.

All simulations were performed on a GPU cluster using the CUDA version of PMEMD (Particle Mesh Ewald Molecular Dynamics) in Amber18 (AMBER 2018, University of California, San Francisco). The protein was modeled with the ff14SB protein force field (26), ligands with the GAFF2 force field (24) and lipids with the AMBER Lipid17 force field. The constructed system was first energy minimized for 10,000 steps, of which the first 5,000 steps were performed using the steepest descent method and the remaining 5,000 steps used the conjugate gradient method. Then the simulation system was heated from 0 to 100 K using Langevin dynamics with a constant box volume. Restraints were applied to protein, ligands, and lipids with a constant force of 10 kcal/mol/Å^2. Subsequently, the temperature was increased to 310 K, where the periodic box was coupled accordingly using anisotropic Berendsen control in order to maintain the pressure at around 1 atm. These restraints were then removed from lipids and the system was equilibrated for another 10 ns at the constant pressure and temperature ensemble (NPT). Further equilibration was then carried out at 310 K with harmonic restraints applied to the protein starting at 5 kcal/mol/Å^2 and reduced in a stepwise fashion every 2 ns for 10 ns, followed by 0.1 kcal/mol/Å^2 restraints for 20 ns for a total of 30 ns of equilibration. Then 2 μs production simulations with no restraints were performed at 310 K and 1 bar in the NPT ensemble for each system. The Particle mesh Ewald (PME) method (Darden et al., 1993) was used to treat all electrostatic interactions beyond a cutoff of 9 Å. The SHAKE algorithm (Ryckaert et al., 1977) was used for recording the length of bonds involving hydrogen during the simulation with an integration time step of 2 fs.

Snapshots from each trajectory were saved every 40 ps during the production runs and these trajectories were used for analysis with Visual Molecular Dynamics (VMD) (27) and CPPTRAJ (28).

Metadynamics Simulations

To investigate the ligand-binding processes and ligand selectivity, we introduced well-tempered metaMD simulations. We choose two collective variables for our simulations: (1) distance between the mass center of a ligand and that of the binding pocket; (2) distance between the mass center of N-terminal and that of ECL2 loop. All membrane systems were built in CHARMM-GUI (Jo et al., 2008), under Charmm36m force field (Huang et al., 2017). Each system contains 132 POPC lipids, 14400 water molecules as well as 0.15 M NaCl. For the details of metaMD simulations, please see our previously published work (Chan et al., 2018; Yuan et al., 2016).

Cyclic AMP Accumulation Assay

Inhibition of forskolin-stimulated cAMP production was measured using the CISBIO® cAMP Homogeneous Time-Resolved Fluorescence Resonance Energy Transfer (HTRF) (FRET) HiRange assay kit according to the manufacturers protocol (Cisbio Assays, Bedford, MA). CHO-hCB2 cells were plated in low-volume 384-well plates (4000/well) using Opti-MEM supplemented with 1% FBS following suspension in 5mM EDTA/PBS. Cells were treated for 30 min with 25μM of phosphodiesterase inhibitor (RO-20-1724), 20μM forskolin, and test compounds. Compounds were dissolved and diluted in DMSO to a final concentration of 1%. Plates were developed by adding the cAMP-d2 antibody and the cryptate solution in lysis buffer for 60 min at room temperature. Fluorescent measures were acquired at 620/665 nm using a Perkin-Elmer EnVision plate reader (Weltham, MA) and FRET was calculated as the 665/620 ratio. In all experiments, 1% DMSO was used as the vehicle and the response was normalized to the percent of response produced by the full agonist CP55,940. Agonist and antagonist drug additions were made at the same time.

QUANTIFICATION AND STATISTICAL ANALYSIS

The determination of agonist potency and relative efficacy was determined by 3 parameter nonlinear regression with responses normalized to the E_{max} produced by CP55,940 in each individual experiment (N = 7 individual assays performed in duplicate) to generate the % CP55,940 graphed in the figure. The determination of antagonist affinity was calculated using a modified version of Schild's method of dose-ratio comparison. At concentrations higher than 10 nM, SR144528 caused a decrease in the baseline activity of the system. It was therefore necessary to include this effect when analyzing the antagonist-mediated shift in the agonist EC_{50}. Specifically, the bottom of the curve was permitted to float freely and the x-value of each response curve was interpolated

where 50% of the maximum response was achieved. The dose-ratio of these interpolated values was used to produce the linearization and estimates of antagonist affinity. All analyses were performed using Prism 8.1 (GraphPad).

DATA AND CODE AVAILABILITY

Data Resources

Coordinates and structures factors have been deposited in the Protein Data Bank for CB2-AM12033 (PDB: 6KPC), CB2-AM12033-G_i-scFv16 (PDB: 6KPF) and CB1-AM841-G_i-scFv16 (PDB: 6KPG).
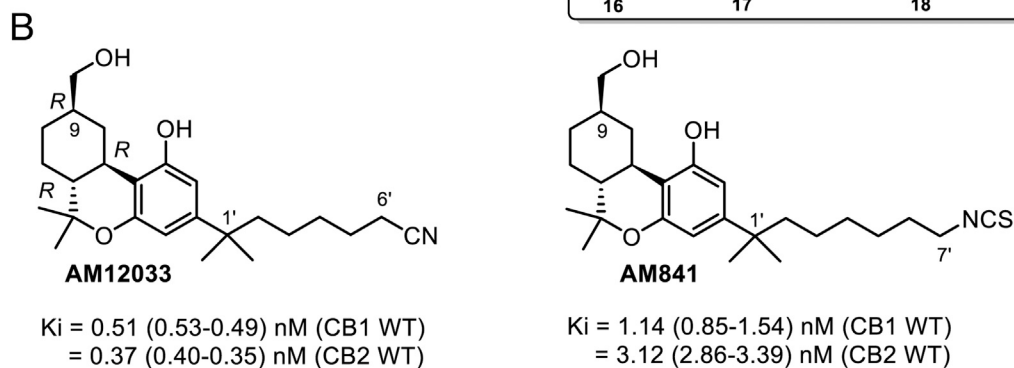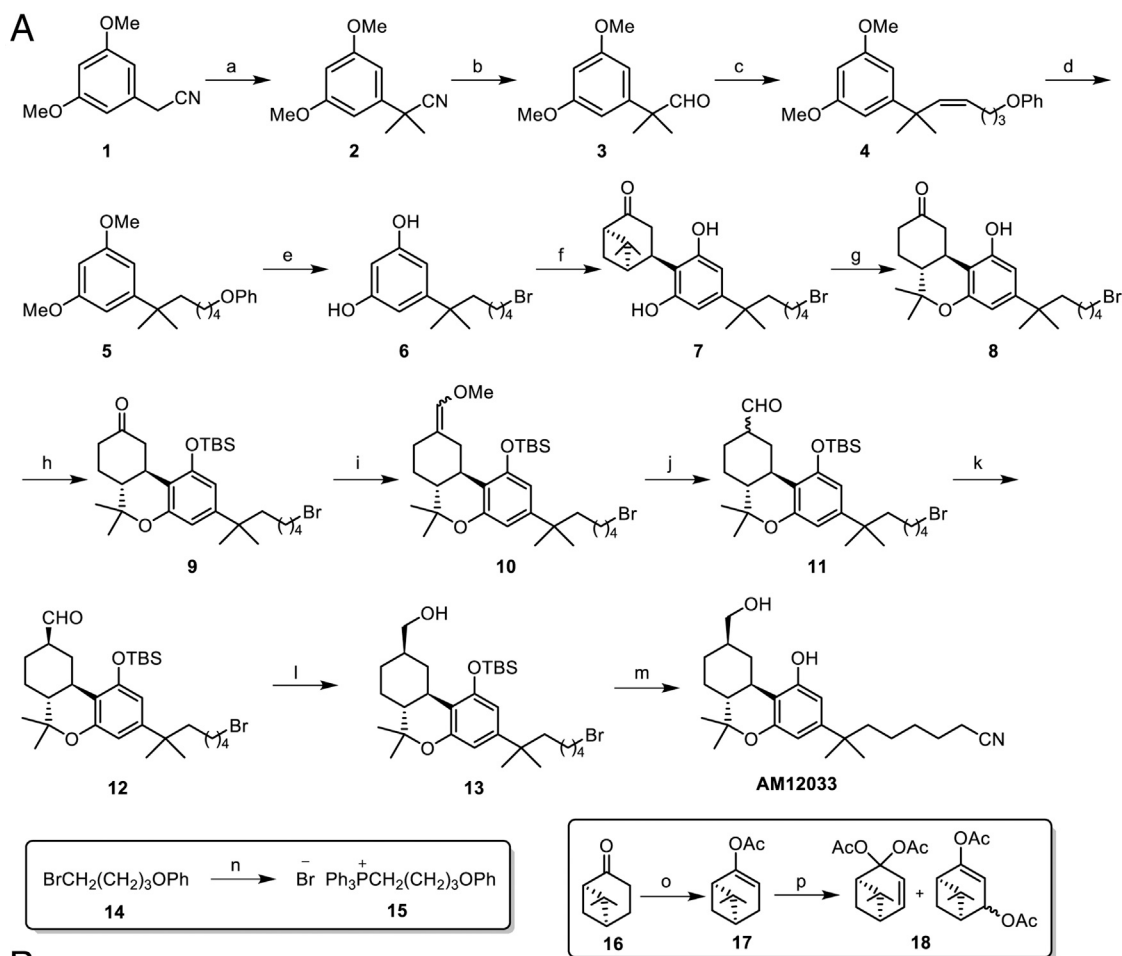
Figure S1. Synthesis of AM12033 and Radioligand Binding Affinities of AM12033 and AM841 against [³H]CP55,940, Related to Figures 1, 2, and 4

(A) Synthesis of AM12033. Reagents and Conditions: (a) CH₃I, NaH, DMF, 0°C to rt, 2 h, 96%; (b) DIBAL-H, CH₂Cl₂, -78°C, 30 min, 92%; (c) 15, (Me₃Si)₂NK, THF, 0 to 10°C, 30 min, then addition to 3, 0°C to rt, 20 min, 96%; (d) H₂, 10% Pd/C, AcOEt, rt, 2.5 h, 98%; (e) BBr₃, CH₂Cl₂, -78°C to rt, 3 h, 99%; (f) 18, *p*-TSA, CHCl₃, 0°C to rt, 4 d, 59%; (g) TMSOTf, CH₂Cl₂/MeNO₂, 0°C to rt, 3 h, 75%; (h) TBDMSCl, imidazole, DMAP, CH₂Cl₂, rt, 12 h, 83%; (i) Cl⁻Ph₃P⁺CH₂OMe, (Me₃Si)₂NK, THF, 0°C to rt, 30 min, then addition to 9, 0°C to rt, 1.5 h, 71%; (j) Cl₃CCOOH, CH₂Cl₂, rt, 50 min, 93%; (k) K₂CO₃, EtOH, rt, 3 h, 81%; (l) NaBH₄, EtOH, 0°C, 30 min, 96%. (m) NaCN, DMSO, rt, 9 h 79%; (n) PPh₃, benzene, reflux, 48 h, 85%; (o) isopropenyl acetate, *p*-Toluenesulfonic acid, reflux, 6 h, 97%; (p) Pb(OAc)₄, benzene, 78–80°C, 3.5 h; 90%.

(B) Structures and radioligand-binding affinities of AM12033 and AM841 against [³H]CP55,940. The assays were performed according to standard procedures (Hua et al., 2016; Li et al., 2019; Liu et al., 2018).
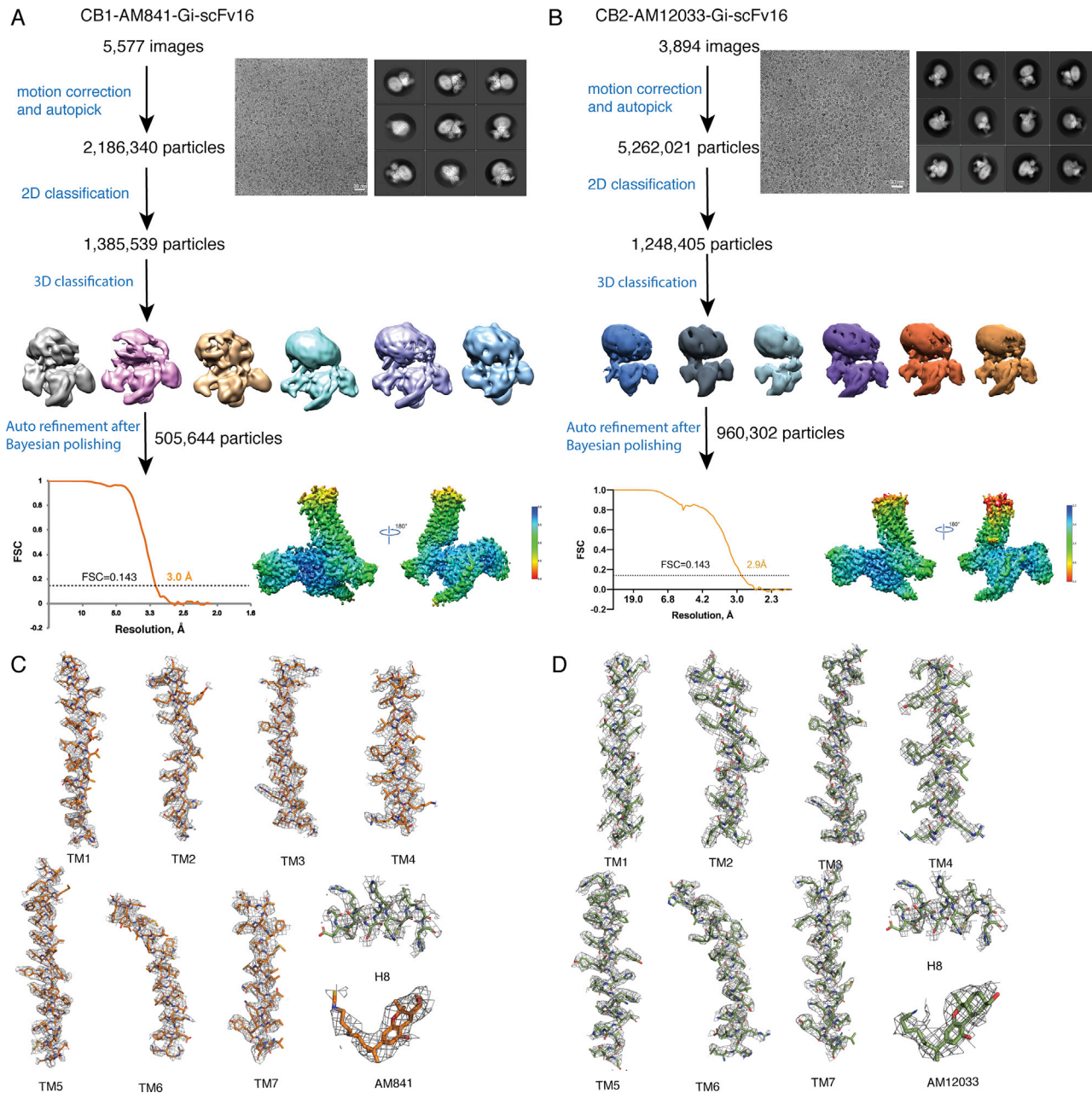
Figure S2. Flowchart of Cryo-EM Data Analysis of the CB1-G$_i$-scFv16 and CB2-G$_i$-scFv16 Complexes, Related to Figure 1

(A) CB1-AM841-G$_i$-scFv complex data processing and refinement, 'Gold-standard' Fourier shell correlation curves indicating the resolution at the FSC = 0.143 is 3.0 Å.

(B) CB2-AM12033-G$_i$-scFv complex data processing and refinement, 'Gold-standard' Fourier shell correlation curves indicating the resolution at the FSC = 0.143 is 2.9 Å.

(C and D) EM density map and model are shown for all CB1 (C) and CB2 (D) transmembrane helices, helix VIII, and ligands.
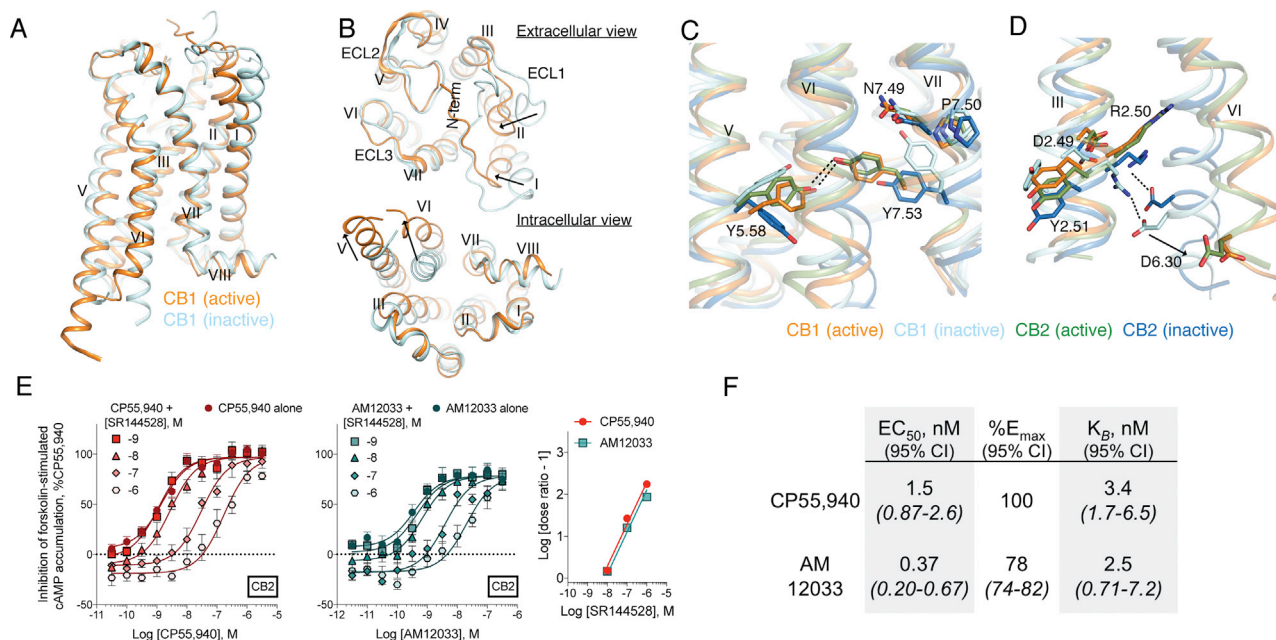
CB1 (active) CB1 (inactive) CB2 (active) CB2 (inactive)

Figure S3. Conformational Changes of DRY and NPxxY Motifs between Inactive and Active CB1 and CB2, Related to Figures 2, 4, and 5

(A) Comparison of CB1 between active and inactive (PDB: 5TGZ) from side view.

(B) Extracellular and intracellular views of superimposed CB1. Active and inactive CB1 are colored in orange and gray, respectively.

(C–D) Comparison of NPxxY (C) and DRY (D) motifs between inactive and active CB1 and CB2.

(E–F) SR144528 is competitive against CP55,940 and AM12033 in the forskolin-stimulated adenylyl cyclase assay (E). Agonist potency and antagonist affinity estimates are provided in (F) (with the K_B derived using Schild Dose-ratio linearization). Since the antagonist displays significant inverse agonism, we also show the linear regression of the Log [dose ratio- 1] using the interpolated 50% of maximum effect and presents the linear fit accounting for the change in baseline. (E) Data points are presented at the mean with SEM for 7 experiments performed in duplicate or triplicate as previously described (Li et al., 2019). The summarized data in (F) are presented as the mean with 95% confidence intervals.
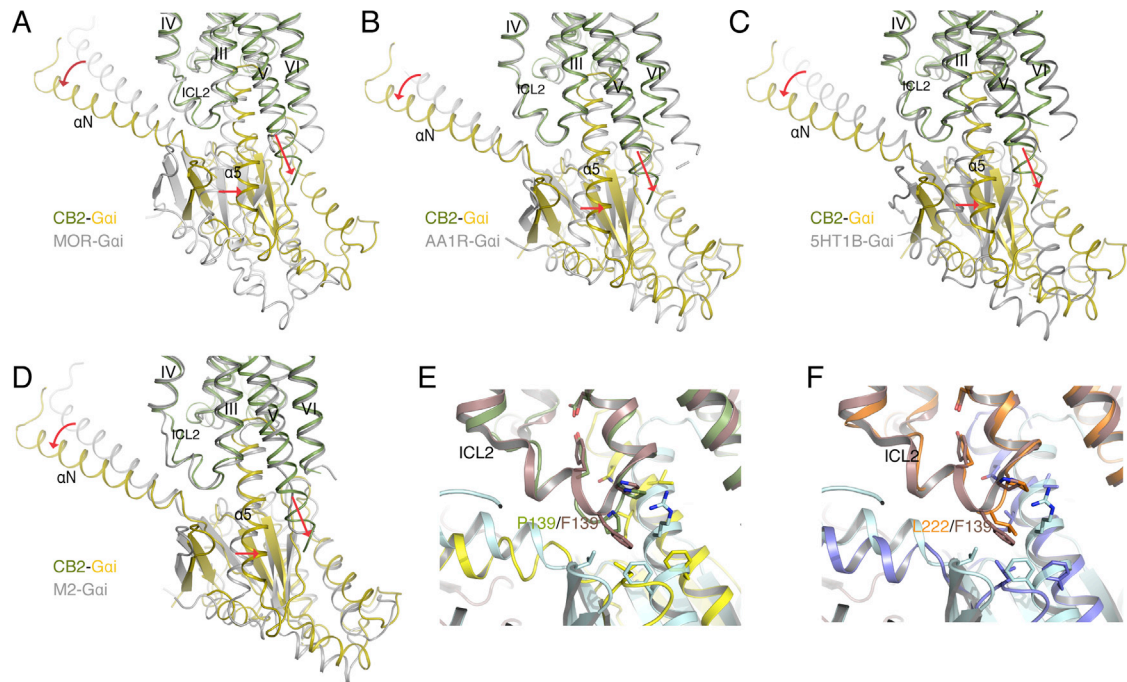
Figure S4. Comparison of the G Protein Orientations between CB2-G$_i$ and GPCR-G$_i$ Complexes, Related to Figure 3

(A) Structure of each GPCR-G$_i$ complex was superimposed onto CB2-G$_i$ based on the receptor component. MOR (PDB: 6DDE).

(B) A1 adenosine (PDB: 6D9H).

(C) 5HT1B (PDB: 6G79).

(D) M2 (PDB: 6OIK).

(E–F) Comparison of the G protein orientation and ICL2 interactions between CB2-G$_i$ (E) and CB1-G$_i$ (F) and β_2AR -G$_s$ complexes.
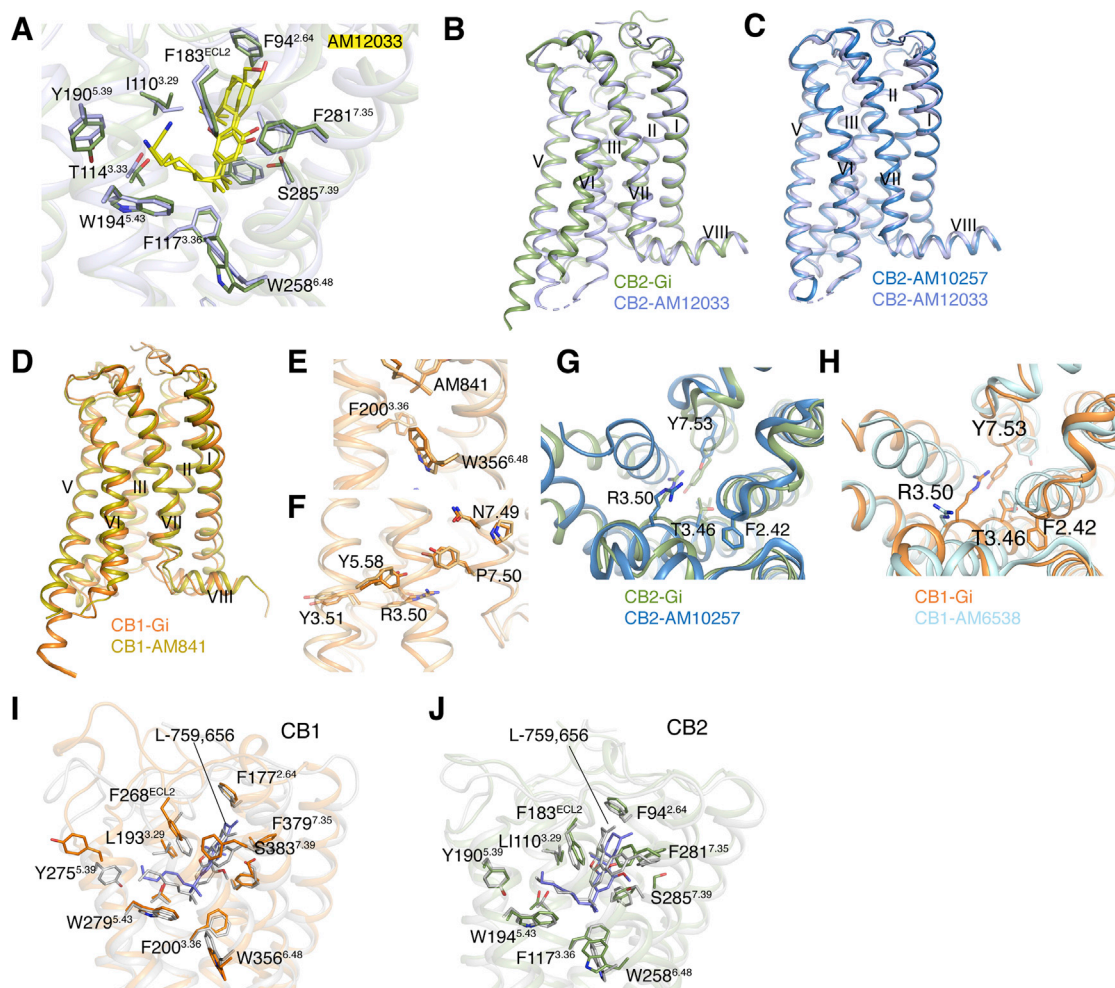
Figure S5. Comparison of the Antagonist, Agonist-Bound, and Active States of CB1 and CB2, and Docking and MD Simulations of L-759,656 in CB1 and CB2, Related to Figures 5 and 6

(A) Binding pose comparison of AM12033 (yellow sticks) in AM12033-bound, light blue; and AM12033-Gi-CB2, green, structures.

(B) Comparison of CB2 between active, green cartoon; and agonist-bound, sky blue cartoon, states from the side view.

(C) Comparison of CB2 between agonist-bound, light blue cartoon; and inactive (PDB: 5ZTY), sky blue cartoon, from the side view.

(D) Comparison of CB1 between active, orange cartoon; and agonist-bound, olive cartoon, states from the side view.

(E) Comparison of "twin toggle switch" between active, orange cartoon; and agonist-bound, olive cartoon, CB1.

(F) Comparison of NPxxY and DRY motifs between active, orange cartoon; and agonist-bound, olive cartoon CB1.

(G and H) The conformational rearrangement around Thr3.46 in CB2 (G) and CB1 (H).

(I) The initial docking pose of L-759,656, gray sticks, in CB1, gray cartoon. After 2 μs MD simulation, L-759,656 is shown as slate sticks and CB1 is shown as orange cartoon.

(J) The initial docking pose of L-759,656, gray sticks, in CB2, gray cartoon. After 2 μs MD simulation, L-759,656 is shown as slate sticks and CB2 is shown as green cartoon.